Detection of directional interactions between neurons from spike trains

Irene Malvestio

TESI DOCTORAL UPF / 2018

DIRECTORS DE LA TESI:

Prof. Dr. Ralph G. Andrzejak[1], Prof. Dr. Roberto Livi[2],

[1]Department of Information and Communication Technologies, Universitat Pompeu Fabra, Spain
[2]Department of Physics, University of Florence, Italy

Acknowledgments

I would like to express my gratitude to my supervisor Ralph G. Andrzejak, for his patient and constant support. He dedicated lot of time for helping me, and he encouraged me to express my ideas and develop my curiosity.
I thank Thomas Kreuz for the fruitful collaboration in my staying in Florence, all the help and support, and for the nice hiking trips.
I thank my supervisor Roberto Livi for supporting me.
I would also like to thank the members of the committee, and the referees who gave me precious help.

I am thankful to Arkady Pikovsky, Antonio Politi and Michael Rosemblum for making COSMOS possible and for sharing their precious knowledge.
I thank also all the other PIs of the COSMOS consortium.
COSMOS would not have been possible without the constant help of Caroline, who was doing an incredible job and make us feeling really supported through the difficulties.

I thank Florian Mormann and Johannes Niediek for sharing data and being so welcoming in Bonn.
I would like to thank also Rodrigo Rocamora and Adrià Tauste Campo for the fruitful collaboration.

I thank my colleagues from COSMOS, with whom I shared nice scientific collaborations but also strong friendships.
Thank you Marc for creating a relaxed and fun atmosphere every time you are around, and for translating the abstract in Catalan.
A special thanks is for Federico, who has been like a brother in these years, and with him the house has been a place for presentation training in the sofa, sharing emotional dilemma, and philosophical discussions.
I would like to thank also my colleagues at UPF. Petroula made the beginning of my PhD a smooth transition, with her love and caring.
Thanks to Cristina, Giulia, Ola for the friendship and the scientific collaborations.
Thanks to Mario and Marco for the coffee breaks.
Thanks to Txema for the help with the thesis format.
Thanks to the students who worked in our group: Minia, Adría, Raul, Andrea.
Thanks to Selma and Heloisa for the inspiring conversations in Santorini.

Thanks to Babita, I cannot find words to describe how precious and inspiring is our friendship for me.
Thanks to Venkatesh for the sweet music.

Grazie alla mia famiglia, e ai miei nonni, che mi insegnano la semplicitá, il rispetto e l'amore.
Grazie ai miei genitori che mi supportano sempre e credono in me, qualsiasi cosa io faccia, aiutandomi a conoscere la libertá.

Abstract

An important problem in neuroscience is the assessment of the connectivity between neurons from their spike trains. One recent approach developed for the detection of directional couplings between dynamics based on recorded point processes is the nonlinear interdependence measure L. In this thesis we first use the Hindmarsh-Rose model system to test L in the presence of noise and for different spiking regimes of the dynamics. We then compare the performance of L against the linear cross-correlogram and two spike train distances. Finally, we apply all measures to neuronal spiking data from an intracranial whole-night recording of a patient with epilepsy. When applied to simulated data, L proves to be versatile, robust and more sensitive than the linear measures. Instead, in the real data the linear measures find more connections than L, in particular for neurons in the same brain region and during slow wave sleep.

Resum

Un problema important en la neurociència és determinar la connexió entre neurones utilitzant dades dels seus trens d'impulsos. Un mètode recent que afronta la detecció de connexions direccionals entre dinàmiques utilitzant processos puntuals és la mesura d'interdependència no lineal L. En aquesta tesi, utilitzem el model de Hindmarsh-Rose per testejar L en presència de soroll i per diferents règims dinàmics. Després comparem el desempenyorament de L en comparació al correlograma lineal i a dues mesures de trens d'impulsos. Finalment, apliquem totes aquestes mesures a dades d'impulsos de neurones obtingudes de senyals intracranials electroencefalogràfiques gravades durant una nit a un pacient amb epilèpsia. Quan utilitzem dades simulades, L demostra que és versàtil, robusta i més sensible que les mesures lineals. En canvi, utilitzant dades reals, les mesures lineals troben més connexions que L, especialment entre neurones en la mateixa àrea del cervell i durant la fase de son d'ones lentes.

Paraules clau: Trens d'impulsos, connectivitat, anàlisi de sèries temporals no lineals, sincronització generalitzada, neurones Hindmarsh-Rose, oscilladors acoblats, epilèpsia, gravacions neuronals d'unitat única.

Contents

List of Figures

List of Tables

CHAPTER 1

Introduction

The detection of dependence between dynamics from experimental signals is very important for the understanding of a wide variety of systems. One of the fundamental problems in the study of brain dynamics is the reconstruction of networks from some measured signals [33]. These signals can be at the macroscopic level, including the electroencephalogram (EEG) the magnetoencephalogram (MEG) [40, 93, 117] and the functional magnetic resonance imaging (fMRI) [103]. Looking at the microscopic level allows one to resolve the activity of individual neurons interacting in networks. From the study of those signals it is hard to reconstruct anatomical links (*anatomical connectivity*) between distinct brain areas. The types of brain connectivity that are studied in the literature are described as *functional* and *effective* connectivity [33]. Functional connectivity is quantified with measures of statistical dependencies, while effective connectivity corresponds to the parameters of a model that tries to explain observed dependencies [33]. In this thesis we focus on the detection of functional connectivity from spike train signals, following a data-driven approach. Differently from other measures of correlation though, the approach that we study was developed focusing on the detection of weak directional interactions between nonlinear dynamics.

The formalism of the analysis of spike trains came originally from the study of point processes, and the hypothesis that spike trains participate in neural coding was developed alongside [113]. In fact, the assumptions are

that individual spikes are indistinguishable from one another [94]. With the same formalism of stochastic point processes [94], in [95] Perkel et al. discussed the basis of the statistical analysis of two simultaneously observed trains of neuronal spikes. The fundamental question was if two spike trains are independent. They use the idea that under the null hypothesis that two spike trains are independent, the times of spike occurrence in one train represent random instants in time with respect to the other. After these initial studies, many different approaches for the detection of driver-response relations between two point processes have been developed. They are usually some extension of concepts applied to the detection of directionality between continuous signals [93]. The first methods were based on cross-correlation [2, 41, 96]. Other methods are adaptations of information theory approaches [28, 45, 69], they evaluate for example the information transfer [39] or the transfer entropy [46, 89, 119]. Granger causality assesses the coupling by evaluating the ability of one spike train to forecast patterns in the other one [52, 61, 81]. There are methods based on maximum likelihood [21, 87, 120], and other methods aim at reconstructing network structure of many neurons assuming to know the underlying node dynamics [16, 86, 97, 124].

In this work we focus on a different class of approaches to detect couplings that is derived from the study of low-dimensional deterministic chaotic dynamics [14], and which are based on the asymmetric state similarity criterion [15]. These measures of nonlinear interdependence [10, 15, 100, 111] quantify the likelihood that similar states of the response are mapped to similar states of the driver. The word *nonlinear* indicates that these measures were specifically designed for being able to detect weak coupling between nonlinear dynamics [6, 18]. The basic assumptions of these approaches is that there are two separate deterministic dynamics which both exhibit an independent self-sustained motion [18]. The other assumptions are that if there is a coupling it is unidirectional and that the dynamics are stationary for the time window under investigation. This approach has later been called also convergent cross mapping [121].

The measure that we use is called L, and it is a particular rank-based and normalized implementation of the asymmetric state similarity criterion. This measure was shown to be of higher sensitivity and specificity for couplings than previous approaches [18]. Methods based on this principle were applied not only in neuroscience [3, 37, 102], but also in other fields, e.g. musical interactions, ecology, climatology etc. [43, 91, 121]. While initial applications were restricted to time-continuous signals, L was subsequently extended to the study of point processes and also to the combination of point processes

and flows [6]. The original method for time-continuous signals is based on a reconstruction of the signals in an embedding space [109], and similarity is assessed by the squared Euclidean distance in that space [18]. Instead, in the application to point processes, the similarity between different windows of the signals is quantified by a spike train distance [54]. The method is modular, meaning that different methods for estimating spike train similarity can be used in order to focus on specific properties of the signals, and also different nonlinear interdependence statistics can be applied.

In the paper where the measure L was first adapted to point processes [6], the capability of the method to detect unidirectional couplings was demonstrated on two model systems, the Lorenz dynamics and Hindmarsh-Rose model neurons. However, only one spike train distance was used, and the analysis was performed under rather simplified conditions. There was no noise and only one possible regime of the Hindmarsh-Rose dynamics was covered (irregular spiking in the driver neuron and bursting in the response neuron). In this thesis we go a decisive step further and using Hindmarsh-Rose dynamics we test the method under more challenging conditions [73]. In Chapter 2 we first test the robustness of the method against different types of noise which are meant to mimic different conditions encountered in the analysis of real data. Subsequently we investigate its behavior in more problematic Hindmarsh-Rose regimes, not only irregular spiking and bursting, but also regimes close to periodicity and exhibiting generalized synchronization. We still use a model system because it allows us both to simulate realistic experimental conditions and to validate the results under controlled conditions. Throughout the analysis, we test different spike train distances, ISI- and SPIKE-distance (Appendix A) in order to understand their advantages and disadvantages.

Considering the conceptual complexity of the measure L, it is interesting to compare its performance against the classical linear cross-correlogram. In Chapter 3 we introduce a framework with temporal shifts (that we call *cross*-functions) that allows this comparison, using again different settings of Hindmarsh-Rose dyamics. We also include the linear spike train distances in the comparison. We do so because spike train distances were specifically designed to quantify spike train similarity. In Appendix A we describe them in detail in their recently introduced adaptive versions [108]. In the comparison we also show interesting properties of *auto*-functions, i.e. the *cross*-functions between a signal and itself. We use time shifts for detecting effective delay of the coupling [23], and *cross*-functions as surrogate techniques.

Finally in Chapter 4 we apply the nonlinear measure L, cross-correlogram and ISI- and SPIKE-distance to spike trains from intracranial recordings of an epilepsy patient. We study a night multi-channel recording of neuronal spiking [82]. We carry out the comparison between the methods using the same framework of Chapter 3, and we illustrate the difficulties that can arise in the analysis of real neuronal data.

Robustness and versatility of the measure *L*

In this Chapter we closely follow our study [73]:
I. Malvestio, T. Kreuz, & R. G. Andrzejak. *Robustness and versatility of a nonlinear interdependence method for directional coupling detection from spike trains*. Physical Review E, 96(2), 022203, 2017.

2.1 Asymmetric state similarity criterion

The method that we use to detect the presence of a coupling is based on the asymmetric state similarity criterion [15]. We consider two unidirectionally coupled dynamics, the driving dynamics X and the response dynamics Y. The criterion is based on the fact that as a consequence of the unidirectional coupling, similar states of Y are likely to be mapped to similar states of X. At first sight, this appears counterintuitive, because it may seem that similar states in the driver should be mapped to similar states in the response. To understand the general idea better we describe a simple example, the interdependence between the weather (driving dynamics) and the behaviour of a girl called Alice (response dynamics). We consider just two states for both driver and response, the weather is either rainy or sunny, and Alice either carries an umbrella or does not. Whenever Alice goes out with an umbrella (similar states of Alice's dynamics) the weather is rainy (similar states of weather dynamics). But if it is rainy, Alice does not always behave

in the same way. For example, she might stay at home, with no need to use an umbrella. Hence, when the coupling is unidirectional, there is an asymmetry in the probability that similarity in one signal implies similarity in the other. This asymmetry is exactly what the asymmetric state similarity criterion uses to detect the direction of the coupling. The degree of the mapping between similar states was used to quantify the strength of the interaction between the driver and the response [4, 18]. Importantly, if the dynamics are close to synchronization, there can be a strong bidirectional mapping between the similarity in the two signals, without a pronounced asymmetry in the two directions. The strong state similarity would be an evidence of high coupling, and the lack of asymmetry would weaken directionality detection [90]. We now describe how L was used in Ref. [6] to apply this principle to spike train signals. First of all, it is necessary to have two signals $x(t)$ and $y(t)$ measured simultaneously from X and Y, respectively. We assume that the two systems are both stationary. In order to make use of the asymmetric state similarity criterion, we need to define the states of the dynamics. In the case of time-continuous signals, the states are obtained by the state space reconstruction of the signals. They contain information about the present and recent past amplitude of the signal [100]. For spike trains, the analogous is to consider short windows. In order to obtain pairs of isochronous windows, we cut the signals in short overlapping pieces.

After defining the states of the dynamics, we need to assess the similarity between different states of the same signal, across different times. For this purpose, we calculate a matrix with the values d_{ij}^X (d_{ij}^Y) of a chosen spike train distance (see Section 2.4) between all pairs of windows i and j ($i, j = 1, \ldots, N_w$, where N_w is the total number of windows) of the signals X (Y).

2.2 The nonlinear interdependence measure *L*

Here we describe the algorithm to calculate the nonlinear interdependence measure *L* proposed by Chicharro and Andrzejak [18]. This measure evaluates the asymmetric state similarity criterion by quantifying the degree to which similarity between states of one dynamics is mapped to similarity between states of the other dynamics. It was already widely applied to time-continuous real-world signals, for example in the study of EEG [3, 37, 102], and also in contexts different from neuroscience [91].

In the previous Section we defined d_{ij}^X. Here we are interested in com-

paring similarity between windows relative to similarity between other pairs of windows. Therefore, we consider ranks of distances instead of exact values of distances. For every window i of the Y dynamics, $i = 1, \ldots, N_w$, we define the quantity r_{il}^Y, which is the index of the window with rank l when sorted by the distance d_{ij}^Y, $j = 1, \ldots, N_w$. We also define $g_{i,m}^X$ as the rank of the distance d_{im}^X in the sorted ascending list of the distances d_{ij}^X, $j = 1, \ldots, N_w$. This allows us to calculate the Y-conditioned mean rank:

$$G_i^k(X|Y) = \frac{1}{k} \sum_{l=1}^{k} g_{i,r_{i,l}^Y}^X. \tag{2.1}$$

This quantity reflects the degree to which the first k closest neighbors of the window i in Y are mapped to close neighbors of the same window in X. The number of nearest neighbors k can be $k \geq 1$, but it has to be small compared to the total number of windows N_w. To estimate the interdependence between the dynamics, we take an average across all windows of a normalized value for $G_i^k(X|Y)$. In this way we obtain $L(X|Y)$ [18]:

$$L(X|Y) = \frac{1}{N_w} \sum_{i=1}^{N_w} \frac{G_i(X) - G_i^k(X|Y)}{G_i(X) - G^k(X)}, \tag{2.2}$$

where

$$G^k(X) = \frac{k+1}{2} \tag{2.3}$$

is the minimal mean rank. $G_i(X)$ is the mean rank expected for independent dynamics

$$G_i(X) = \frac{M_i + 1}{2}. \tag{2.4}$$

The value M_i is the number of windows taken into account for comparing similirairy. We exclude from the comparison W windows close to the diagonal, because they correspond to neighbouring windows on time: $M_i = N_w - 2W - 1$ for $W < i < N_w - W + 1$, whereas below and above this range, M_i increases linearly until it reaches the values $M_1 = M_{N_w} = N_w - W - 1$. This is in analogy to the Theiler correction [123].

The measure $L(X|Y)$ has the expected value 0 for independent dynamics. When the coupling strength from X to Y increases, also $L(X|Y)$ increases. The maximum possible value is $L(X|Y) = 1$, reached when X and Y are equal or so similar that their matrices of ranks of distances coincide. The measure L is designed such that $L(X|Y)$ detects the coupling from X to

Y. To quantify the level of coupling in the other direction, we use $L(Y|X)$, obtained by switching the role of X and Y in Eq. 2.2 and in all previous definitions. We use $\Delta L(X,Y) = L(X|Y) - L(Y|X)$ to assess the direction of the coupling [18].

The modularity of the approach based on the asymmetric state similarity criterion allows one to choose a statistics different from L to evaluate the criterion. In the context of time continuous signals other nonlinear interdependence measures were proposed [5, 10, 111]. Here we consider only L because it was shown [18] to be more sensitive and specific for directional couplings than previous approaches.

2.3 Spike train distances

In the last twenty years, many different measures of spike trains similiarity were developed [54]. Among the best-known are the Victor-Purpura distance [127] and the van Rossum distance [125]. Both depend on a parameter that defines the time-scale to which the method is mainly sensitive to. This sensitivity determines the relative importance of rate versus exact timing of the spikes in computing the dissimilarities. Kreuz et al. developed the ISI-distance [57] and the SPIKE-distance [56], two time-scale independent, time resolved distances which can evaluate dissimilarity without the need of having to set a time-scale.

These distances were applied not only in neuroscience [11, 38, 79], but also in other fields [130]. Recently, new generalizations of these distances were developed [108], called A-ISI-distance and A-SPIKE-distance. These generalized definitions add a notion of the relative importance of local differences compared to the global time-scales. In particular, they start to gradually ignore differences between spike trains for interspike intervals (ISIs) that are smaller than a minimum relevant time-scale.

We here give a brief description of three measures of spike train synchrony [54]: the time-scale dependent van Rossum distance [125], and the time-scale independent ISI- and SPIKE-distances in their adaptive generalizations [56, 57, 108]. For a more detailed description of the time-scale independent measures see Appendix A.

2.3.1 van Rossum spike train distance

For the van Rossum distance, each spike time t_n^1 ($n = 1, \ldots, N_s^1$, where N_s^1 is the number of spikes in this spike train) is convolved with an exponential kernel, giving the convolved waveform:

$$f_1(t) = \sum_{t_n^1=1}^{N_s^1} H(t - t_n)e^{-(t-t_n)/\tau_R},$$

where $H(t)$ is the Heaviside step function. The time constant τ_R is a parameter that sets the time scale. Analogous formulation holds for the convolved waveform $f_2(t)$ of second spike train, with spike times t_n^2 ($n = 1, \ldots, N_s^2$, where N_s^2 is the number of spikes in the second spike train, which can be different than the number of spikes in the first spike train). The van Rossum distance D_R [125] is then calculated as:

$$D_R(\tau_R) = \frac{1}{\tau_R} \int_0^\infty [f_1(t) - f_2(t)]^2 dt. \tag{2.5}$$

For high values of τ_R the distance between the two spike trains is mostly determined by the difference in rate (since timing differences get lost in the smoothed convolutions), while for low τ_R the temporal relationship between the spike timing is taken more into account (since even small differences in spike time lead to a significant contribution).

2.3.2 ISI- and SPIKE-distance

Both the ISI- and the SPIKE-distance compute first a time-resolved spike dissimilarity profile [77]. The ISI-dissimilarity-profile $I(t)$ is based on the interspike intervals, whereas the SPIKE-dissimilarity-profile $S(t)$ takes into account the exact timing of the spikes. Here we briefly describe how to compute these two dissimilarities profiles, using the notation of Mulansky et al. [77].

The ISI-dissimilarity-profile $I(t)$ is based on the relative length of simultaneous interspike intervals [57]. For every time t let $t_P^{(1),(2)}(t)$ be the time of the last preceding spike, and $t_F^{(1),(2)}(t)$ be the time of the first following spike, for the first and the second spike train, respectively. The instantaneous interspike interval is thus defined as: $\nu^{(1)}(t) = t_F^{(1)} - t_P^{(1)}$, and analogously for

$\nu^{(2)}(t)$. The profile $I(t)$ is computed by normalizing the absolute difference of the interspike intervals:

$$I(t) = \frac{|\nu^{(1)}(t) - \nu^{(2)}(t)|}{\max\{\nu^{(1)}(t), \nu^{(2)}(t)\}}. \tag{2.6}$$

By construction $\nu^{(1)}(t)$ and $\nu^{(2)}(t)$ are piecewise constant functions, and the same holds for $I(t)$.

The SPIKE-dissimilarity-profile focuses on the exact timing of spikes. For every time t, the distance from the last preceding spike to the closest spike of the other spike train is defined as:

$$\Delta t_P^{(1)}(t) = \min_i \{|t_p^{(1)} - t_i^{(2)}|\}$$

and analogously for $\Delta t_P^{(2)}$ and $\Delta t_F^{(1),(2)}$. Then these values are weighted by the instantaneous distances to the two nearest spikes:

$$x_P^{(1)}(t) = t - t_P^{(1)},$$

$$x_F^{(1)}(t) = t_F^{(1)} - t$$

with $x_P^{(1)}(t) + x_F^{(1)}(t) = \nu^{(1)}(t)$. In this way the local dissimilarity is obtained as

$$S_1(t) = \frac{\Delta t_P^{(1)}(t) x_P^{(1)}(t) + \Delta t_F^{(1)}(t) x_F^{(1)}(t)}{\nu^{(1)}(t)}, \tag{2.7}$$

and $S_2(t)$ is defined analogously.

The SPIKE-dissimilarity-profile $S(t)$ is obtained from these local distances $S_1(t)$, $S_2(t)$, weighted by the local interspike intervals, with a final normalization:

$$S(t) = \frac{S_1(t)\nu^{(2)}(t) + S_2(t)\nu^{(1)}(t)}{2\langle \nu^{(1,2)}(t)\rangle^2}. \tag{2.8}$$

Notice that $S(t)$ is a piecewise linear function.

For both the ISI- and the SPIKE-distance the total distance between two spike trains is then calculated as an integration over time of the instantaneous spike dissimilarity profile:

$$D_P = \frac{1}{t_e - t_s} \int_{t_s}^{t_e} P(t)dt, \quad P = I, S,$$

10

where t_s and t_e are the beginning and the end of the interval.

In the calculation of the dissimilarity profiles there is always an ambiguity concerning the interval preceding the very first and following the very last spike. In our case we initially calculate the profile for the whole time series and afterwards we segment it in overlapping windows and compute the integrals. This way, for the intermediate windows we use some information about the spikes in neighbouring windows, and the problem remains only at the very beginning and at the very end of the spike trains. For this reason we ignore the first and the last W_{ex} windows of our signals. The value of W_{ex} is set adaptively as the minimum number of windows that we have to neglect in order not to consider windows with empty neighbour windows.

Recently adaptive generalizations of the ISI- and the SPIKE-distance were proposed [108], which take into account the relative importance of local differences compared to the global time-scale (see Appendix A for a more detailed description). By relying on a minimal relevant time scale, they basically give less importance to the differences that are smaller than a threshold $\mathcal{T}$. This threshold is computed as the mean of the square root of the second moments of the ISIs of the whole spike train. It is important to calculate $\mathcal{T}$ for each spike train from the whole signal and not just from individual windows, in order to compute a meaningful distance between different windows of the same signal. In contrast, $\mathcal{T}$ can in general be different for the two spike trains whose connection is under investigation. In fact, the measure L evaluates how similarity between different windows of one signal is mapped on similarity among different windows of the other signal.

In this thesis, we only show the values of L computed with the adaptive generalization of ISI- and SPIKE-distance. Their property of taking into account the global information about the time scale and not only adapting to the local one is always desirable [108]. Additionally, in particular for L_{SPIKE} this is also reflected in a higher robustness to noise.

2.4 Assessing similarities between states with spike train distances

Since it is not defined *a priori* which should be the proper 'distance' between different windows of a spike train, we study different possible choices: We apply the van Rossum distance and the generalizations of ISI- and SPIKE-

distance (see Section 2.3). To distinguish between L computed with different distances, we use the notation L_{ISI} when A-ISI-distance is used, L_{SPIKE} for the A-SPIKE-distance and L_{vR} for the van Rossum distance. In pre-analysis the Victor-Purpura distance yielded very similar results to the van Rossum distance and is thus omitted here. When the parameter of the van Rossum distance increases, the distance focuses more on spike rate than spike timing accuracy. On the one hand the parameter offers more flexibility, but on the other hand it is not obvious how to adjust it. Regarding the two parameter-free distances, we exploit the fact that A-ISI-distance focuses on differences of the rate whereas the A-SPIKE-distance focuses more on the exact timing, in order to gain complementary information about the system. In Figure 2.1 we present an exemplary application of the three spike train distances to both the driver X and the responder Y of a unidirectionally coupled system. This example illustrates that the three distances give complementary information.

Segments of the signal of a fixed length q are used as states of the dynamics for the calculation of the distance matrices. In order to obtain a finer sampling, we use overlapping windows, i.e. from one window to the next there is a step size s with $s \leq q$, which leads to the following segmentation of the signal: $[(i-1)s, (i-1)s + q]$ with $i = 1, \ldots, N_w$. The total duration of the point process is Q, and the total number of windows N_w is obtained by rounding down $\frac{Q-q}{s} + 1$. In every window, the time τ of a spike is relative to the beginning of the segment: $\tau = t - (i-1)s$, where t is the time of the spike relative to the beginning of the whole signal. We mentioned in Section 2.2 that in the distance matrices, for every reference window we exclude the comparison with the W overlapping neighboring windows, in analogy to the Theiler correction [123]. A possible value for W is $W_{min} = \frac{q}{s} - 1$, which is the minimal one that guarantees to avoid the comparison between overlapping windows. It is important to choose the parameters of the method properly. In general, a good choice for q is the length of several mean interspike intervals, because a minimum number of spikes in every window is needed for a good evaluation of distances between windows. The parameter s should be a good trade-off between having more sensitive results (shorter s) and the required computation time (which is shorter for larger s).
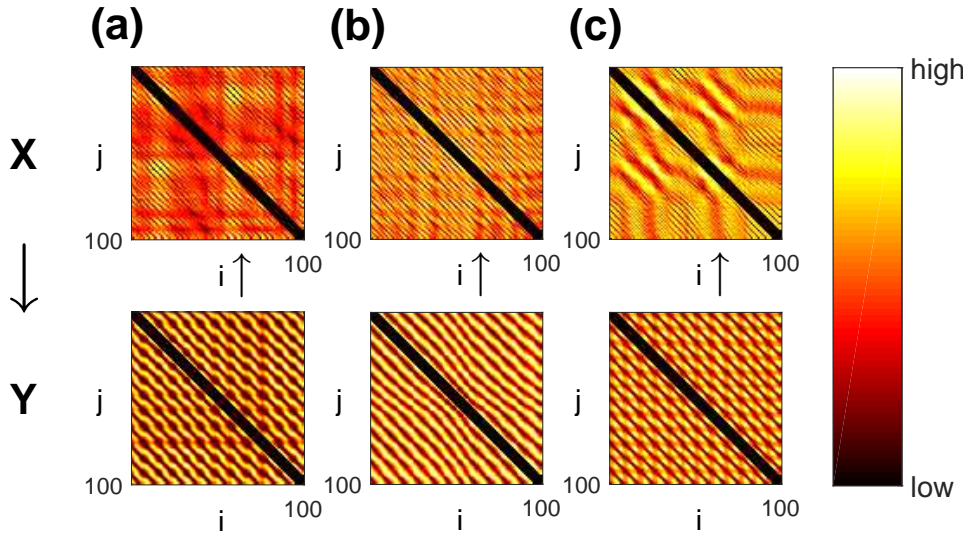
Figure 2.1: Example of distance matrices d_{ij}^X (first row) and d_{ij}^Y (second row) calculated with three different spike trains distances: (a) van Rossum distance, (b) SPIKE-distance, (c) ISI-distance. The signals are simulated from unidirectionally coupled Hindmarsh-Rose dynamics X and Y (driver and response, as indicated by the large arrow). The matrices are quite different even for the same signal. From the asymmetric state similarity criterion we expect that dark colour in the d_{ij}^Y matrices are likely to correspond to dark colour in the d_{ij}^X matrices, as indicated by the direction of the small arrows. Elements close to the diagonal are not taken into account (see Section 2.4).

2.5 Methods

2.5.1 Test on simulated data: Hindmarsh-Rose neurons

We use spike trains derived from coupled Hindmarsh-Rose model neurons ([49] and references therein) to test different methods. This model is the same as in [6], but here we consider more complicated settings. The system of equations is composed of a driver dynamics X

$$
\begin{aligned}
\dot{x}_1(t) &= x_2(t) + 3x_1(t)^2 - x_1(t)^3 - x_3(t) + J_x \\
\dot{x}_2(t) &= 1 - 5x_1(t)^2 - x_2(t) \\
\dot{x}_3(t) &= 0.0021(-x_3(t) + 4(x_1(t) + 1.6)),
\end{aligned}
\tag{2.9}
$$

and a response dynamics Y,

$$
\begin{aligned}
\dot{y}_1(t) &= y_2(t) + 3y_1(t)^2 - y_1(t)^3 - y_3(t) + J_y \\
&\quad + \epsilon Z(x_1(t))(0.3 - y_1(t)) \\
\dot{y}_2(t) &= 1 - 5y_1(t)^2 - y_2(t) \\
\dot{y}_3(t) &= 0.0021(-y_3(t) + 4(y_1(t) + 1.6)).
\end{aligned}
\tag{2.10}
$$

The coupling strength is ϵ and the coupling function is defined as

$$
\dot{Z}(x_1(t)) = \frac{Z_\infty(x_1(t)) - Z(x_1(t))}{100(1 - Z_\infty(x_1(t)))}
\tag{2.11}
$$

with

$$
Z_\infty(x_1(t)) = \begin{cases} \tanh\left(x_1(t) + 0.5\right), & \text{if } x_1(t) > -0.5, \\ 0, & \text{else.} \end{cases}
\tag{2.12}
$$

The two dynamics are identical apart from the input currents J_x and J_y, which moreover determine the dynamical regime of the signals. The type of coupling (Eq. 2.11-2.12) is a model for chemical synapses, whereas electrical synapses are described by a diffusive coupling [99]. The first components of Eqs.2.9 and 2.10 represent the membrane potential of the neurons. In experiments, often one cannot measure the membrane potential but only the times of spikes. To simulate such experimental conditions, here we extract from these two time-continuous signals the spike times that compose the point processes X and Y. The time of the spike is the instant in which the signal $x_1(t)$ crosses a threshold from below. As the

threshold value we chose $\Theta = 0.6$. We call t_n^X the time of the n-th spike, with $n = 1, \ldots, N_s^X$ and N_s^X being the total number of spikes in X. The times t_n^Y are defined analogously.

The Hindmarsh-Rose equations were integrated with a fourth-order Runge-Kutta algorithm. The step size was 0.1 time units and the sampling step $\Delta t = 0.2$ time units. We define $T = 1000\Delta t$ as the unit time interval. We started the dynamics with random initial condition and the first $500T$ was discarded to exclude initial transients of the dynamics. The length of the spike trains was $Q = 400T$, and for the segmentation of the signals we used a window length of $q = T$ with an overlap of $s = 0.2T$. We chose a Theiler window W of $W_{min} = \frac{q}{s} - 1$. In order to avoid any type of in-sample optimization, this procedure was exactly the same as in the previous work [6].

Depending on the parameters J_x and J_y, there can be different dynamical regimes of the Hindmarsh-Rose model: spiking or bursting regimes, and both can be periodic or aperiodic. In general the resulting signals have different numbers of spikes, and furthermore the number of spikes in the response changes with increasing coupling. In our work we analyze two settings. In Setting A, we use the same regime as in [6], to test the robustness against noise for the different spike train distances. In Setting B, we consider different input currents and coupling values in order to validate the method for a range of different problematic dynamical regimes, as dynamics close to periodicity and under generalized synchronization.

An example of the signals from Setting A is shown in Figure 2.2, with irregular spikes in the driving dynamics and irregular bursts in the response. The input currents are the same as in [6], $J_x = 3.30$ and $J_y = 3.28$. We computed L for the uncoupled case plus $n_\epsilon = 29$ coupling values ϵ equidistantly distributed on a logarithmic scale from 0.0006 to 0.24. For each ϵ, we run $n_r = 20$ independent realizations of the dynamics. We say that the coupling and its direction for a specific value of ϵ is detected if the mean of the difference on the n_r realizations $\langle \Delta L(X, Y) \rangle = \langle L(X|Y) - L(Y|X) \rangle$ is significantly larger than zero. In order to assess the significance, we performed a Wilcoxon signed rank test on $\langle \Delta L(X, Y) \rangle$. The level of significance was $\alpha = 0.05/n_\epsilon$, where we used the Bonferroni correction [114] to take into account the multiple testing of the n_ϵ values of the coupling. We use this setting to study the robustness of the measure L to noise. We define the performance Ψ to be the percentage of the n_ϵ coupling values for which we can significantly detect the coupling and its direction. To quantify the variability of Ψ, we ran three times n_r realizations and we calculated

the mean and the variance of the performances. When we compare the performance for the robustness to noise with different spike train distances, for the ISI-distance and the SPIKE-distance there is no need of choosing a parameter. Instead, in the case of the van Rossum distance, we compute the performance Ψ for a range of parameters and we select the one which leads to the best performance.

In Setting B we consider different input currents ($J_x = 3.28$, $J_y = 3.60$). We consider the uncoupled case plus $n_\epsilon = 89$ coupling values ϵ equidistantly distributed on a logarithmic scale from $6 * 10^{-6}$ to 1.8. Here the driving dynamics is in an irregular bursting regime, while the response shows a variety of different behaviours. It is close to periodicity for very small coupling values (Figure 2.3a), while it undergoes a bifurcation as the coupling increases, until it reaches an irregular bursting regime (Figure 2.3b). Finally, for the highest coupling values, there are degenerated bursts (Figure 2.3c): the spikes in the bursts show a decrease in the amplitude from the beginning to the end of the burst, and the amplitudes of the last ones are so small that the spikes do not reach the threshold for detection any longer. The very irregular shape of the spikes makes them not so well-defined as in the other regimes, and even adjusting the threshold would not be effective. Therefore, as the coupling increases, the detected spikes preserve less and less of the information contained in the time-continuous signals. There are two intervals of coupling values for which the driving and the response are in generalized synchronization [105]. The concept of generalized synchronization comes from the study of time-continuous signals. Two dynamics X and Y are in generalized synchronization when the trajectories $y(t)$ of Y can be derived by a functional relationship from the corresponding trajectories $x(t)$ of X [53]. In this way, $y(t)$ is not dependent anymore on its initial conditions. In order to check for which coupling values the dataset is in the regime of generalized synchronization, we use the auxiliary system approach [1], exploiting the fact that the spike trains that we study are extracted from time-continuous signals. For a realization of the driving dynamics X [Eq. 2.9] we generate two realizations of the response dynamics, Y and Y', which obey the same equations 2.10 but start from different initial conditions. We wait a long transient ($50000T$) and we compute the average of the difference between the last $400T$ of $y_1(t)$ and $y_1'(t)$. If this distance is zero that means that the Y dynamics is independent of its initial condition, therefore generalized synchronization is established.

16
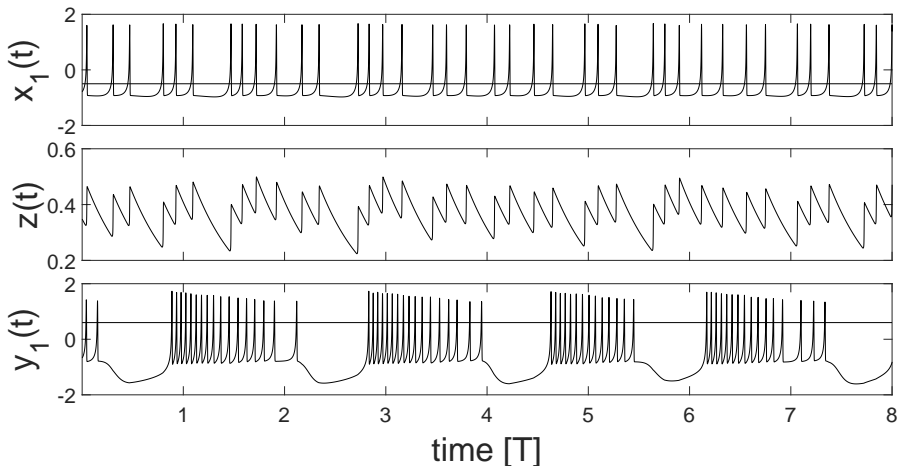
Figure 2.2: Example signals for Setting A: coupled Hindmarsh-Rose dynamics $(x_1(t), y_1(t))$ with coupling strength $\epsilon = 0.24$, $J_x = 3.30$ and $J_y = 3.28$. The coupling function $z(t)$ is defined as $z(t) := Z(x_1(t))$ (see Eq. 2.11). Horizontal lines represent the threshold for spike detection. The time is in unit of T. The $x_1(t)$ signal is in an irregular spiking, the $y_1(t)$ signal in an irregular bursting regime.

2.5.2 Robustness to noise

In this Section we introduce different noise types that we apply to the simulated signals of Setting A. We select them in order to cover some of the principal disturbances that can affect data in the real world. The principal noise sources are due to the intrinsic stochasticity of the neurons [30, 50], the uncertainty due to spike sorting and other measurement noises [68].

At first we consider a noise type which we call *unreliability noise*. It represents the possibility of having false-positive and false-negative detections of spikes. We simulated this noise by randomly removing and inserting spikes. In the original point process t_n^X, with $1 \leq n \leq N_s^X$, we remove $0 \leq M \leq N_s^X$ spikes. At the same time, we randomly insert M new spikes. The positions of the new spikes are uniformly distributed in the interval between 0 and the total recording time Q. This way, the new spike train $\tilde{t}_n^X$ has the same number N_s^X of spikes, while the interspike interval distribution is not maintained. We define the noise level γ_u as the fraction of spikes that we remove and insert $M = \gamma_u N_s^X$. Analogous definitions hold for the t_n^Y spike train.

The second type of noise is a shift in the spike times, the *jitter noise*. In this case, we shift every spike time of both t_n^X and t_n^Y by a different
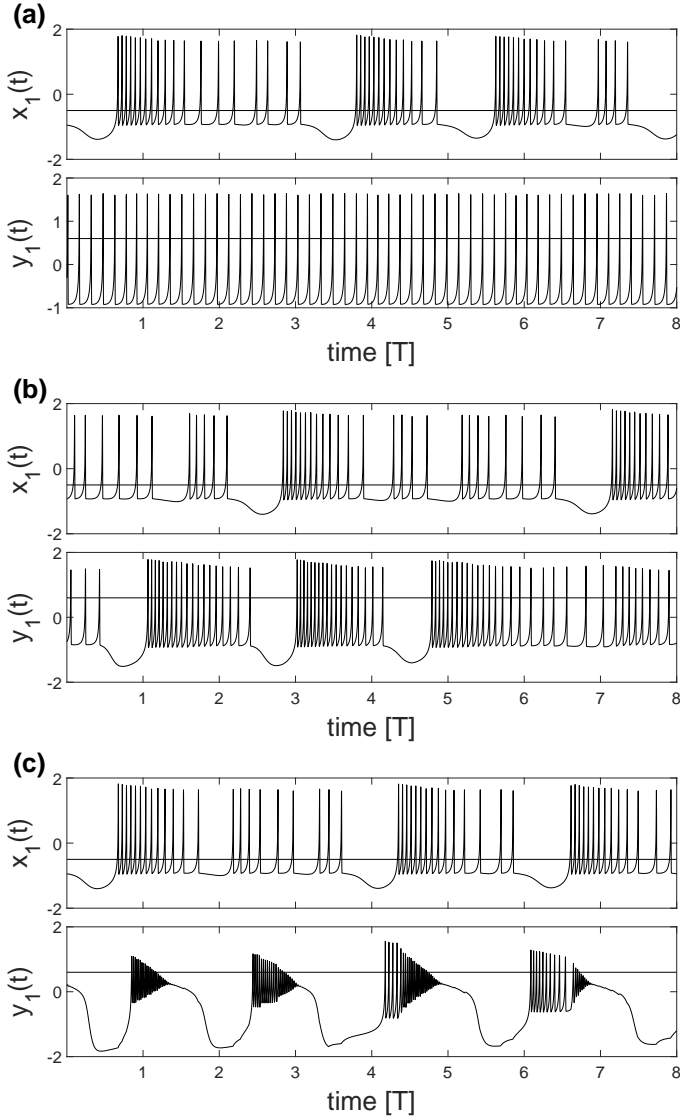
Figure 2.3: Example signals for Setting B: coupled Hindmarsh-Rose dynamics $(x_1(t), y_1(t))$ with $J_x = 3.28$ and $J_y = 3.6$. In all the panels, the $x_1(t)$ signal is in an irregular bursting regime. The time is in unit of T. The $y_1(t)$ signal is very close to periodicity in panel (a), where the coupling strength is $\epsilon = 0.0101$, in an irregular bursting regime in panel (b), $\epsilon = 0.1092$, and finally it presents degeneration of the bursts in panel (c), $\epsilon = 1.0276$.

delay δt extracted from a Gaussian distribution with zero mean and standard deviation σ. We choose σ as a fraction γ_j of the mean interspike interval of

18

the time series μ_{ISI}: $\sigma = \gamma_j \mu_{\text{ISI}}$. The noise level is quantified by γ_j.

The third type of noise reflects the fact that spike propagation depends on unreliable connections between neurons, for example some spikes of two connected neurons may not be transmitted. We represent this effect by modifying a term in the equations, hence it is a dynamical noise that we call *transmission noise*. In the Hindmarsh-Rose Eqs. 2.9-2.12 the coupling between the neurons is mediated by the coupling function $Z(x_1(t))$ [Eq. 2.11], which is influenced by $x_1(t)$ only when $x_1(t)$ is higher than the threshold of -0.5, i.e. in correspondence to a spike in x_1. We cancel the influence from single spikes of X on Y, with some probability γ_t, which quantifies the noise level. Thus, for the whole time of the increase of the membrane potential due to a specific spike in x_1, we let the function Z evolve as if the threshold was not crossed. It is important to notice that by ignoring spikes we reduce the "effective" coupling strength.
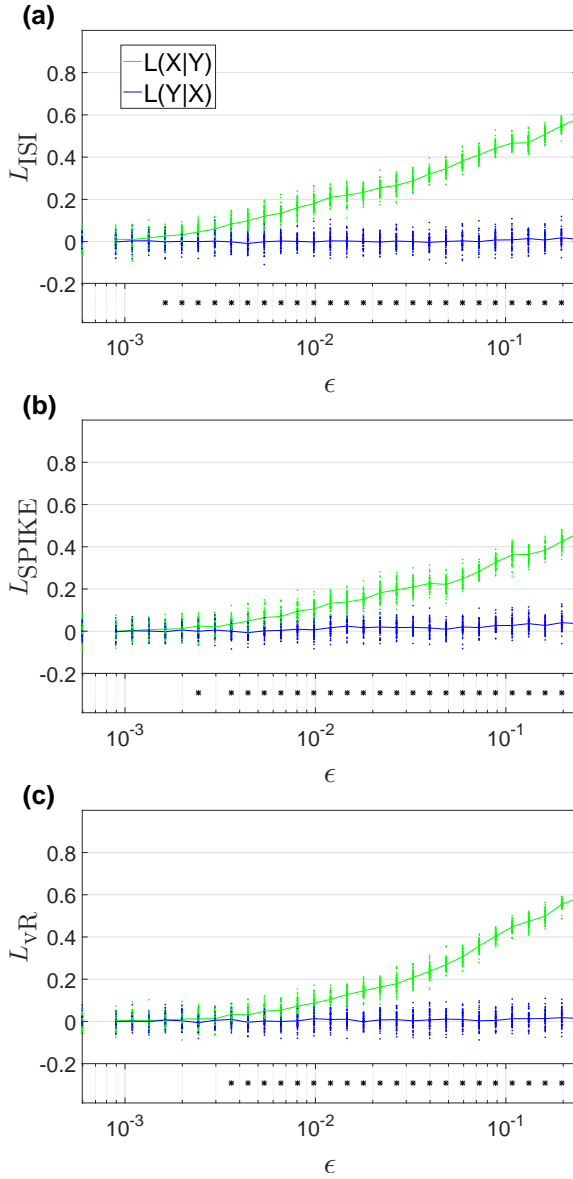
Figure 2.4: Values of L for increasing coupling strength (the number of nearest neighbors k of Eq. 3.17 is set as $k = 1$). From top to bottom, L_{ISI}, L_{SPIKE} and L_{vR} (with the optimal parameter for significant coupling detection). For every coupling value, there are 20 independent realizations. Results for uncoupled dynamics ($\epsilon = 0$) are displayed on the ordinates. The stars on the bottom of the plots mark the coupling values for which the detection of the coupling is significant. The measure L_{ISI} performs best, since it is able to detect even low couplings.
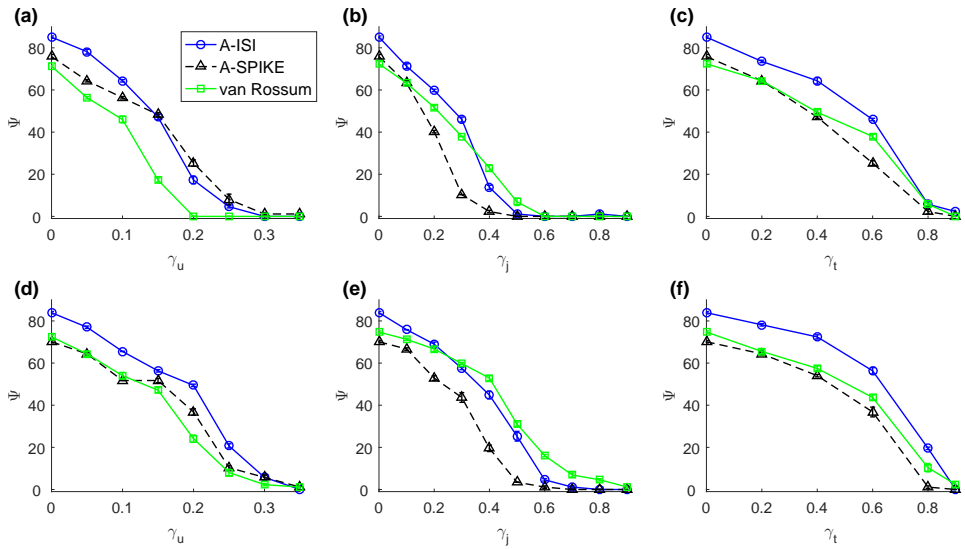
Figure 2.5: Comparison of the performance Ψ of the measure L for different spike train distances in dependence on increasing levels of (a, d) *unreliability*, (b, e) *jitter* and (c, f) *transmission noise*. In the first row (a, b, c) we set $k = 1$, in the second row (b, e, f) $k = 10$. The A-ISI-distance performs best. The robustness to noise is improved by a higher number of nearest neighbors k.
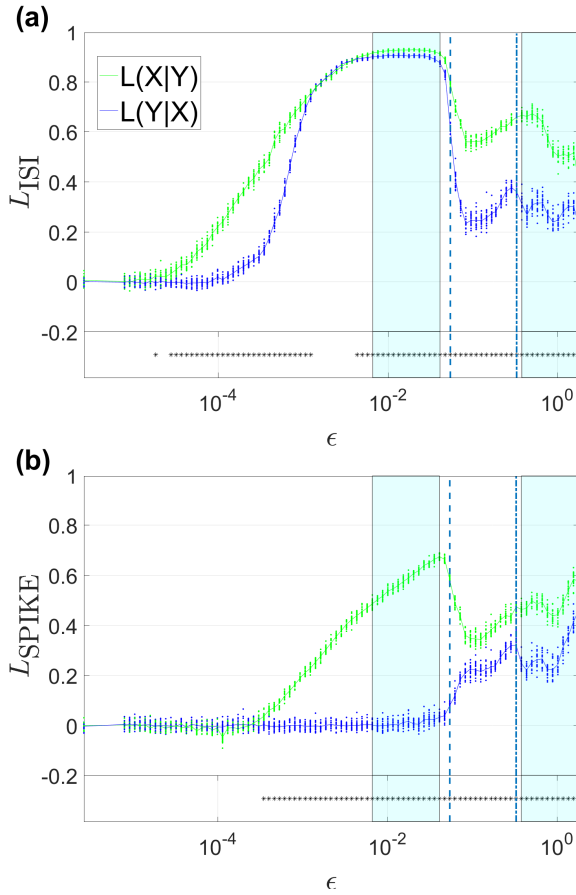
Figure 2.6: Values of L_{ISI} and L_{SPIKE} in dependence on the coupling strength ϵ ($k = 10$). Results for uncoupled dynamics ($\epsilon = 0$) are displayed on the ordinates. The stars on the bottom of the plots mark the ϵ values for which the direction of the coupling is significantly detectable. The shaded areas correspond to the generalized synchronization regimes. The first dashed vertical line on the left distinguishes the regime close to periodicity (corresponding to small coupling values, see Figure 2.3a) from the regime with bursts in the response (see Figure 2.3b), and the second line marks the transition to the regime for which there is a strong degeneration of the bursts (see Figure 2.3c).
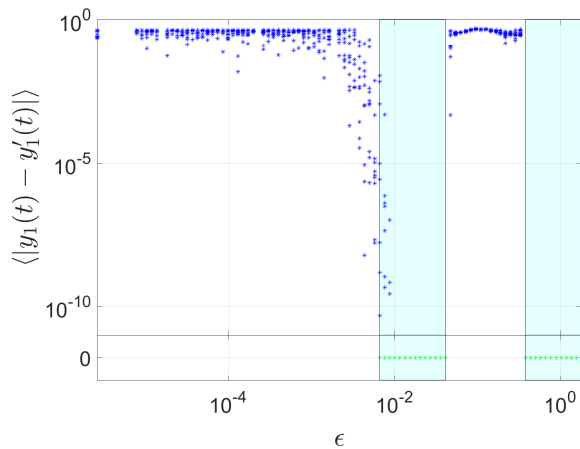
Figure 2.7: Results of the auxiliary system approach applied to Setting B of the Hindmarsh-Rose model. We plot the average of the absolute value of the difference between the last $400T$ corresponding values of $y_1(t)$ and its copy $y'_1(t)$, after discarding a transient of 10^5T. For every coupling value there are five independent realizations, each of them represented by an asterisk. The green crosses at the bottom that correspond to values of exactly zero in at least one realization mark the regime of generalized synchronization. Results for uncoupled dynamics ($\epsilon = 0$) are displayed on the ordinates.

2.6 Results

In this Section we show the influence of different distances and parameters on the efficiency of L. First we study the dependence on the coupling strength without noise. Subsequently, we investigate the robustness of L to various kinds of noise. Finally, we test the versatility of this approach to work in different dynamical regimes.

We start our analysis with the noise-free case of Setting A. In Figure 2.4 we investigate the dependence of L on the coupling strength for the A-ISI-distance (L_{ISI}), the A-SPIKE-distance (L_{SPIKE}) and the van Rossum distance (L_{vR}). The measure L_{ISI} can distinguish the direction even for small ϵ and it also gives higher values of L. The measure L_{vR} instead, even with the parameter which optimizes the performance Ψ, performs worse and has lower values than L_{ISI}. The L_{SPIKE} performs worst.

In Figure 2.5 we continue to analyze Setting A, but now we investigate the effect of the different spike train distances on the robustness against noise of L. We also look at the influence of k on the performance. In the presence of *unreliability noise*, generally L_{ISI} continues to perform best, even if for high levels of noise L_{SPIKE} starts to perform better (Figure 2.5a). It is clear that selecting a high number of neighbors is very important for the robustness of the method, since the overall performance increases (Figure 2.5b). At the same time, for $k = 10$, L_{ISI} performs best across the entire range of noise levels. For larger k the value of L in general decreases, but also the variance of L across different realizations decreases because averaging over more neighbors gives more stable results. As a consequence the direction detectability improves, in particular in the presence of noise. The measure L_{vR}, even though its parameter is optimized separately for every noise-level, performs worst. Regardless of the spike train distance, up to 35% of the spikes have to be removed and randomly reinserted in order to completely destroy the performance. Thus we can conclude that the measure L is robust to *unreliability noise*.

For *jitter noise* (Figure 2.5c,d) L_{vR} performs very well, in particular it slightly outperforms L_{ISI} for high levels of noise. Every spike has to be shifted by a value extracted from a Gaussian distribution of standard deviation 70% of the mean interspike interval in order to lead to zero performance. Accordingly, we can state that the method is robust also to *jitter noise*.

The measure L_{ISI} performs best also with the addition of *transmission noise* (Figure 2.5e,f). Despite the optimization, L_{vR} performs worse than L_{ISI}.

The performance is zero only if 90% of the spikes of the driven dynamics are ignored by the coupling, hence the measure L is robust also to *transmission noise*. We notice that in this case the performance stays high for high levels of noise and then it drops more suddenly at the end. The dependence on the noise level is therefore different than for the other noise types.

One interesting aspect of this analysis concerns the strong dependence of the van Rossum distance on the time-scale parameter (results not shown). Putting the focus on rate works better in the presence of high levels of *jitter noise*, whereas for high levels of *unrealiability noise* it is preferable to focus on spike accuracy. This is intuitive and in agreement with the comparison of L_{SPIKE} and L_{ISI} in the presence of these two types of noise. However, this dependence of the optimal parameter on the type and level of noise, renders the use of the van Rossum distance problematic for applications to realistic situations when all kinds of noise are present at the same time and the ground truth is unknown.

In Setting B, we focus on the adaptability of the measure L to spike trains which reflect the different regimes of the underlying dynamical systems (Figure 2.6). To avoid the complications caused by the time-scale parameter, we do not consider the van Rossum distance any longer (and the same applies to the time-scale dependent Victor-Purpura distance). From Figure 2.6a we can see that L_{ISI} is highly sensitive to small coupling values, even if in this regime the response is close to periodicity (compare Figure 2.3a). At the same time, L_{SPIKE} cannot detect the very small coupling values (Figure 2.6b). When ϵ increases, the values of L for both spike train distances increase, but their behaviour differs. The directionality detection of L_{ISI} deteriorates until the values of L_{ISI} are very close to one and almost coincide in both directions. The results of the auxiliary system approach in Figure 2.7 confirm that the high values of L_{ISI} correspond to coupling values close to and inside the first interval of the generalized synchronization regime. Surprisingly, for the corresponding coupling values L_{SPIKE} can perfectly detect both the presence and direction of the coupling.

The behaviour of L_{ISI} resembles the behaviour of L for time-continuous signals when the coupling is approaching a value large enough to induce generalized synchronization [18]. This behaviour is well-known in the study of time-continuous signals [104]. As a consequence, a requirement for the applicability of directionality detection is that the coupling does not induce synchronization [90, 115]. The high sensitivity of L_{ISI} leads more easily to high values for the coupling without any sign of directionality when approaching the regime of generalized synchronization. In contrast,

while being less sensitive, L_{SPIKE} in the generalized synchronization regime can perfectly detect the direction of the coupling. There might be two reasons for these results. First, the rate compared to the exact timing is more easily affected by a small coupling. Second, the functional relation of generalized synchronization which connects the $y_1(t)$ and $x_1(t)$ signals of the Hindmarsh-Rose model can be very complicated, and it is in principle possible that it is easier to detect from spike rate instead of spike timing. A complete study of generalized synchronization between two Hindmarsh-Rose dynamics is beyond the scope of our study. Nevertheless, empirically we see that generalized synchronization expresses itself in different features.

After the first synchronization window, while both values $L_{\mathrm{ISI}}(X|Y)$ and $L_{\mathrm{SPIKE}}(X|Y)$ show a decrease, a distinction of the coupling direction is still possible (Figure 2.6). These coupling values correspond to the change of regime in the response, from almost regular spiking to irregular bursting (compare Figure 2.3b). In this case, the values of L increase also in the opposite direction $L(Y|X)$. We remind that $L(Y|X)$ would indicate a coupling from Y to X. For the highest coupling values, L_{ISI} decreases again in both directions (Figure 2.6a). Furthermore, there is another window of generalized synchronization. However, both L_{ISI} and L_{SPIKE} behave differently as compared to the first window. Here the corresponding signals show an additional effect, the degeneration of the bursts (see Figure 2.3c). The spikes contain less information about the original time-continuous signals. Moreover, spike density in the bursts is very high and there are longer inter-burst periods. This bursting structure leads to smaller values of L despite the higher coupling strength, compared to the previous regime close to periodicity.

2.7 Discussion

The detection of directional interdependence between unknown dynamics from their signals is a non-trivial problem, and in the last decades many different approaches to address this problem have been proposed. Before using a method to interpret real data, it is always important to first study its properties and to apply it to model systems. Thus in this Chapter we simulate realistic experimental conditions to validate a method for the detection of unidirectional couplings between point processes. This approach is based on the asymmetric state similarity criterion in the formulation of the nonlinear interdependence measure L [18]. The capability of this method

to detect coupling was already demonstrated in the Lorenz and in one setting of Hindmarsh-Rose dynamics [6]. Here we examine the robustness against various kinds of noise and the versatility of the approach in dealing with different dynamical regimes. Additionally, we take advantage of the modularity of the measure L and test three spike train distances which are sensitive to different aspects of the dynamics.

Our results show that among the three distances that we used for the measure L, the A-ISI-distance exhibits the highest sensitivity in detecting unidirectional coupling. While all three distances prove to be very robust in the presence of noise, again the measure L_{ISI} performs best. The measure L in general works for different dynamical regimes, including irregular spiking, irregular bursting, almost periodic motion and under generalized synchronization. Interestingly, L_{ISI} and L_{SPIKE} catch different features of the coupling between spike trains, namely an interdependence based on the rate or on exact spike timing, respectively. Therefore, it is recommendable to apply both L_{ISI} and L_{SPIKE}, because they provide complementary information and might therefore be sensitive to different coupling strengths.

In general, the values of L are not monotonically increasing with an increase of the coupling value. As emphasized in [64], the effect of the coupling depends not only on the coupling strength but also on the energy of the individual dynamics. As a consequence, the estimate of the coupling is not independent from the structure of the data, for example in bursting or spiking regimes.

The choice of the parameters is important to obtain meaningful results. In particular, we have seen that a higher number of nearest neighbors k is an advantage in the presence of noise. Nonetheless, no fine-tunig of k is needed, and a value of approximately 0.5% of the total number of windows is a good choice in order to be less affected by noise. Another important parameter is the window length. If it is too long it reduces the reliability of the measure L, in the sense that there will be too few windows to compare. If it is too short, the estimation of similarity is not reliable. In order to obtain robust results, we recommend a minimum number of 5 spikes. Furthermore, the relevant information about similarity can be contained in a complex structure, such as the bursts, which cannot be properly captured by very short windows.

It was shown in the previous study [6] and is further supported by our results that the measure L for the detection of directional coupling between point processes performs well in the study of simulated spike trains derived from nonlinear deterministic dynamics. If the spike trains are from two coupled stochastic point processes instead, the measure L could have trou-

ble with the detection of directionality, even if the presence of a coupling is still detectable. Another caveat is the possibility to have a small but significant difference in the values of L in the two directions also for bidirectionally coupled dynamics [64]. As a consequence, in the interpretation of experimental results, more caution is necessary to assume directionality if $L(X|Y) \approx L(Y|X)$. An open question regards the efficiency of the measure L under these conditions and how to quantify the reliability of directionality detection.

Since different methods can extract information from different features of the data, it is recommendable not to restrict yourself to just one approach such as nonlinear interdependence measures, but instead to use complementary techniques for directionality detection [28, 39, 41, 61, 69, 81, 119, 120]. In the next Chapter we compare the measure L with the cross-correlogram and the spike train distances used for coupling detection. A more comprehensive comparison with also other methods regarding their statistical requirements, their computational cost and their abilities to provide complementary information on the dynamics under investigation will be the focus of future studies.

CHAPTER 3

Comparison of the measure *L* with linear methods

In Chapter 2 we tested the robustness of the measure *L* to noise and its versatility to different spike train regimes of Hindmarsh-Rose dynamics, that manifest themselves in different predominant patterns in the spiking: irregular bursts, irregular spikes, etc. In this Chapter we compare the performance of the nonlinear measure *L* against the one of the linear cross-correlogram [95] and the spike train distances (Appendix A). The measure *L* was introduced relatively recently in [6] and it is a quite complicated method of data analysis. It is therefore important to compare its efficacy against other standard approaches. This comparison is not so trivial considering that the measures rely on different assumptions.

The zero-lag cross-correlogram and spike train distances do not allow to extract the direction of the coupling, because they are symmetric measures. However, a common approach is to look at the cross-correlogram as a function of a time shift between the signals. Here we generalize that approach to the spike train distances and finally also to the measure *L* (even though it is already directional at zero shift). We assume that the difference for the positive and negative temporal shifts reflects the difference between driver and response. In analogy to the expressions *cross*-correlogram and *auto*-correlogram, we use the term *cross* to refer to the case when we compute a measure between two signals, as a function of a time shift between

29

them. The word *auto* instead is referring to the case of a *cross* function between a signal and itself. In application to our measure for nonlinear interdependence, this leads to *cross-L* and *auto-L*. The approach *auto-L* corresponds to the nonlinear predictability score introduced by Naro et al. [80]. We should note that cross-functions for spike train distances were already used before in [13], with the aim of detecting latencies. With the formalism of *cross*-distance, we test for the first time the efficacy of the spike train distances as methods to not only test for the presence of a coupling, but also the direction of the coupling.

In the first part of this Chapter we define the methods that we compare using *cross*- and *auto*-functions. Then we compare their performance for directionality detection simulating many realizations of the same dynamics for the assessment of the significance of the results (Section 3.2). In the second part of the Chapter (Section 3.3) we approach a simulated scenario more similar to the case of real-world data, considering only one realization of each dynamics. In this case we use *cross*-functions as surrogates for assessing the significance of the coupling. Surrogates are Monte Carlo techniques for estimating a distribution of values expected under a certain null-hypothesis [65]. We use them to estimate a distribution of values expected for pairs of independent spike trains. In the application of nonlinear methods to phenomena in nature, surrogates are used to test the nonlinearity of the dynamics [4, 62, 112]. In the context of spike train analysis, there is a wide use of generation of artificial data from experimental ones for implementing null hypothesis. For example, for the correlation analysis of parallel spike trains, often the complexity of data does not allow analytical formulation [71]. Surrogates should preserve as far as possible features such as the inter spike interval distribution [51, 70], non-stationarity of firing rate or irregularity of firing rate [118]. Commonly used methods are trial shuffling, spike time randomization, spike train dithering, spike time dithering, joint-ISI dithering, spike exchanging [41]. In this Chapter we deal with pairs of spike trains and we do not make assumptions on the time scale of the coupling, therefore we choose to use time-shifted surrogates which preserves all characteristics of the individual signals.

3.1 Methods for interdependence and directionality detection

3.1.1 Cross-correlogram and auto-correlogram

The simplest and most intuitive method for computing the dependence between two signals is the cross-correlation [95]. When the signals are spike trains, we obtain the cross-correlogram [24], which is a histogram of the number of spikes of one neuron at a certain time, relative to the spike times of another neuron. It is computed by counting coincidences between the spikes in one signal with the shifted spikes of the other signal, as a function of the time shift. Evidently, it is necessary to use binning to assess the interval for which two spikes are considered coincident. The choice of the bin width is important, because it affects the time scale that we look at. A significant peak close to zero delay in the cross-correlogram is an indicator of interdependence between the signals. If the delay is too far away from zero, taking into account our prior knowledge about the dominant time scales of the system under study, a prominent peak can be interpreted to be a result of chance coincidences. The position and broadness of the peak could point to different types of interrelation. For example, a broad peak may be due to nonstationarity in the firing rates of the neurons which leads to an increase of joint-spike events (if the time-dependent firing rates co-vary in the same way in both spike trains).

There are many different ways to define the cross-correlogram [83, 92] for spike train signals. Here we consider two spike trains $x(t)$ and $y(t)$. We define $x_{\mathrm{count}}(t_C)$ and $y_{\mathrm{count}}(t_C)$ as the number of spikes that occur in the bin with index t_C, with $t_C = 1, \ldots, Q$ and Q total length of the spike trains. We call the bin width f and the step size between two subsequent bins s_C. If $s_C = f$ there is no overlap between subsequent bins. We express the shift τ between $x(t)$ and $y(t)$ in units that we call f_{shift}. In general, f_{shift} is not equal to f. This is an important point that allow us to cover different time-scales. Next, we define the *cross*-correlogram as:

$$\textit{cross-}C(\tau) = \frac{Q}{Q - \tau} \sum_{t_C = \max(0, \tau)}^{\min(Q - \tau, Q)} x_{\mathrm{count}}(t_C) \cdot y_{\mathrm{count}}(t_C - \tau), \qquad (3.1)$$

with $\tau = (-N_{\mathrm{delay(cross)}}, \ldots, N_{\mathrm{delay(cross)}}) \cdot f_{\mathrm{shift}}$, where $N_{\mathrm{delay(cross)}}$ is the total number of positive and negative delays that we compute. The normalization

factor $\frac{Q}{Q-\tau}$ takes into account that the overlap between the two signals is reduced for bigger shifts, and therefore also the likelihood to have simultaneous spikes between them decreases. Similar signals have high values for their *cross*-correlogram for small values of τ.

Let us assume to have two unidirectionally coupled dynamics X and Y. We want to use the *cross*-correlogram to assess the directionality studying their signals $x(t)$ and $y(t)$. A peak at negative delay is an indication of a coupling from X to Y, while a peak at positive delays points to a coupling in the opposite direction. Therefore, we can use as estimator for the two directions:

$$cross\text{-}C(X|Y, \tau) = cross\text{-}C(\tau), \quad \text{with } \tau < 0, \tag{3.2}$$

and

$$cross\text{-}C(Y|X, \tau) = cross\text{-}C(\tau), \quad \text{with } \tau > 0. \tag{3.3}$$

We apply the *standard score* as normalization to these functions, in order to have a distribution with a mean of 0 and a standard deviation of 1:

$$z(x) = \frac{x - \text{mean}(x)}{\text{std}(x)}, \tag{3.4}$$

where the mean $\text{mean}(x)$ and the standard deviation $\text{std}(x)$ are computed across all the delays τ of *cross*-$C(\tau)$ in Eq. 3.1. If we have many realization n_r of the dynamics, the directionality of the coupling is assessed by a significant difference between the maximum values of these two functions:

$$\Delta M_C := M_C(X|Y) - M_C(Y|X) :=$$
$$\max(z(cross\text{-}C(X|Y, -\tau))) - \max(z(cross\text{-}C(Y|X, \tau))),$$
$$\text{with } \tau = (1, \dots, N_{\text{delay(cross)}}) \cdot f_{\text{shift}}. \tag{3.5}$$

We call the position of the maximum $\tau_C^{\max}$. In general, the absolute value is different for the two directions: $|\tau_C^{\max}(X|Y)| \neq |\tau_C^{\max}(Y|X)|$.

The *auto*-correlogram of $x(t)$ corresponds to the *cross*-correlogram (Eq. 3.1) between $x(t)$ and itself:

$$auto\text{-}C(\tau) = \frac{Q}{Q - \tau} \sum_{t_C=\max(0,\tau)}^{Q} x_{\text{count}}(t_C) \cdot x_{\text{count}}(t_C - \tau), \tag{3.6}$$

with $\tau = (0, \dots, N_{\text{delay(auto)}}) \cdot f_{\text{shift}}$, where $N_{\text{delay(auto)}}$ is the total number of positive delays in dependence of which we compute the *auto*-function.

3.1.2 Cross-distances and auto-distances

We consider again two spike trains $x(t)$ and $y(t)$, with $t = 0, \ldots, Q$. We define $d_{ISI}(x(t), y(t))$ and $d_{SPIKE}(x(t), y(t))$ to refer to the A-ISI-distance and A-SPIKE-distance computed between the two signals, using the definitions of Section 2.3 and Appendix A.

Introducing the time shift, we define the *cross*-distances *cross*-ISI and *cross*-SPIKE:

$$cross\text{-ISI}(\tau) = 1 - d_{ISI}(x(t), y(t - \tau)), \qquad (3.7)$$

$$cross\text{-SPIKE}(\tau) = 1 - d_{SPIKE}(x(t), y(t - \tau)), \qquad (3.8)$$

where the distances are computed for the time range $t = \max(0, \tau), \ldots, \min(Q - \tau, \tau)$. The shift τ between the signals $x(t)$ and $y(t)$ is expressed again in units of f_{shift}, $\tau = (-N_{delay(cross)}, \ldots, N_{delay(cross)}) \cdot f_{\text{shift}}$. Here we do not need to include a normalization factor because the spike train distances are already normalized themselves. In Eqs. 3.7 and 3.8 we take one minus the distances in order to get a measure of similarity instead of dissimilarity, analogously to the *cross*-correlogram (Eq. 3.1).

As in Section 3.1.1, to assess the directionality between unidirectionally coupled dynamics, we can use the maximum values for positive and negative delays:

$$cross\text{-distance}(X|Y, \tau) = cross\text{-distance}(\tau), \quad \text{with } \tau < 0, \qquad (3.9)$$

and

$$cross\text{-distance}(Y|X, \tau) = cross\text{-distance}(\tau), \quad \text{with } \tau > 0, \qquad (3.10)$$

and with the *standard score* normalization (Eq 3.1.1) where $\text{mean}(x)$ and $\text{std}(x)$ are computed across all the delays τ of *cross*-ISI(τ) (Eq. 3.7) and *cross*-SPIKE(τ) (Eq. 3.8):

$$\Delta M_D := M_D(X|Y) - M_D(Y|X) := \max(z(cross\text{-distance}(X|Y, -\tau)))$$
$$- \max(z(cross\text{-distance}(Y|X, \tau))), \text{with } \tau = (1, \ldots, N_{\text{delay(cross)}}) \cdot f_{\text{shift}}. \qquad (3.11)$$

We call the position of the maximum $\tau_D^{\max}$, whose absolute values are in general different for the two directions: $|\tau_D^{\max}(X|Y)| \neq |\tau_D^{\max}(Y|X)|$. For the *auto*-distances, analogously to Eq. 3.6, we get:

$$auto\text{-ISI}(\tau) = 1 - d_{ISI}(x(t), x(t + \tau)), \qquad (3.12)$$

$$auto\text{-}\mathrm{SPIKE}(\tau) = 1 - d_{SPIKE}(x(t), x(t + \tau)), \qquad (3.13)$$

where the distances are computed for the time range $t = 0, \ldots, Q - \tau$ and $\tau = (0, \ldots, N_{\text{delay(auto)}}) \cdot f_{\text{shift}}$.

3.1.3 Cross-*L* and auto-*L*

The measure *L* is a measure of nonlinear interdependence which allows one to determine not only the strength but also the direction of this interdependence. The value $L(X|Y)$ is an estimation of the coupling strength from X to Y, while $L(Y|X)$ is for the other direction. This estimation is based on the asymmetric state similarity criterion (introduced in Section 2.1), i.e. if there is a unidirectional coupling from X to Y, similar states in Y are likely to be mapped to similar simultaneous states in X. In this formulation, no delay is considered in the coupling detection. However, note that the states of the signals cannot be instantaneous (in order to be able to meaningfully estimate similarity between them). In the case of continuous signals, the states are based on a reconstruction of the dynamics with delayed coordinates [109, 122], therefore they can be interpreted as instantaneous. In the case of point processes there is no reconstruction, and the temporal length of the states automatically takes into account the possible presence of a latency in the interdependence. Despite this consideration, it is nevertheless meaningful to introduce explicitly small shifts between the signals also for the measure *L*. From the point of view of the asymmetric state similarity criterion, we are thus checking if similar states in Y at time $t_1, t_2, \ldots$ are mapped to similar states in X at time $t_1 + \tau, t_2 + \tau, \ldots$.

As introduced in Section 2.4, we estimate the states of the dynamics with short segments of fixed length q, with an overlap of s, $s \leq q$. As a consequence we get a segmentation of the signal: $[(i - 1)s, (i - 1)s + q]$ with $i = 1, \ldots, N_w$. The total length of the signal is Q, with a total number of windows N_w obtained by rounding down $\frac{Q-q}{s} + 1$.

We define *cross-L* as:

$$cross\text{-}L(X|Y, \tau) = \mathrm{L}(x(t)|y(t - \tau)), \qquad (3.14)$$

$$cross\text{-}L(Y|X, \tau) = \mathrm{L}(y(t)|x(t - \tau)), \qquad (3.15)$$

with $\tau = (-N_{delay(cross)}, \ldots, N_{delay(cross)}) \cdot f_{\text{shift}}$ and L computed for the time range $t = 0, \ldots, Q$. Considering the higher computational complexity of the measure L (compared to the previously defined *cross*-correlogram and *cross*-distances), in the definition of *cross-L* we use circular boundary

condition $x(-t) = x(Q - t)$, $y(-t) = y(Q - t)$, with step f_{shift} always being an integer multiple of s. In this way, we can compute L without the need to re-compute the distance matrix for all time shifts. Instead we can introduce a circular shift by f_{shift}/s matrix elements to the distance matrix. This is equivalent to shifting the signals against each other.

In the case of *cross*-correlogram and *cross*-distances, exchanging the role of x and y only changes the sign of the *cross*-function, i.e., *cross*-$C(X|Y, \tau) =$ *cross*-$C(Y|X, -\tau)$, and analogously for the *cross*-distances. In fact, we introduced the difference between the peaks at positive and negative delays for assessing directionality. We notice that in the case of *cross*-L the same property does not hold: *cross*-$\text{L}(X|Y, \tau) \neq$ *cross*-$\text{L}(Y|X, -\tau)$. We can still use the maximum values of *cross*-L at positive and negative delays as for *cross*-correlogram (Eq. 3.5) and *cross*-distances (Eq. 3.11) to assess the directionality of the coupling, but in this case we take negative and positive delays of different functions:

$$\Delta M_L := M_L(X|Y) - M_L(Y|X) :=$$
$$\max(\text{\textit{cross}-L}(X|Y, -\tau)) - \max(\text{\textit{cross}-L}(Y|X, \tau)),$$
$$\text{with } \tau = (0, \dots, N_{\text{delay(cross)}}) \cdot f_{\text{shift}}. \quad (3.16)$$

We call the position of the maximum $\tau_L^{\max}$. Its absolute values are in general different for the two directions: $|\tau_L^{\max}(X|Y)| \neq |\tau_L^{\max}(Y|X)|$. Another difference to Eqs. 3.5 and 3.11 is that for the measure L we always include also the values of zero τ as possible value of $\tau_L^{\max}$ for both directions.

3.1.3.1 Predictability score

In this Section we describe the rank-based predictability score, a nearest neighbor prediction measure introduced in reference [7] for assessing the determinism in spike train signals. This approach quantifies the auto-predictability of individual signals, since signals derived from deterministic dynamics should exhibit some predictability. Here we use the predictability score for the definition of *auto*-L.

We consider the dynamics Y and the spike train distances d_{ij}^Y between all pairs of windows i and j ($i, j = 1, \dots, N_w$) of the signals (in complete analogy with Section 2.4). From these distances we can determine the degree to which the future states of similar windows are similar between them. For each reference window i, we want to compare its future after h steps, that corresponds to the window with index $i + h$, with the future of

the k most similar windows to i, whose indexes are $r_{i,l}$, with $l = 1, \ldots k$, as in Section 2.2. In analogy to the Theiler correction [123], we do not consider the entries around the diagonal of the distance matrix. That means, for every reference window we exclude the comparison with W temporal neighbouring windows. We also have to exclude the last h windows from the analysis, because their recorded future is not sufficiently long. Therefore, the number of distances is $M_i = N_w - 2W - 1$ for $W < i < N_w - W + 1$, whereas below and above this range, M_i increases linearly until it reaches the values $M_1 = M_{N_w} = N_w - W - 1$, exactly as in the computation of L in Section 2.2. We denote with $g_{i,m}$ the rank of the distance d_{im}^Y in the sorted ascending list of the distances $d_{ij}^Y, j = 1, \ldots, N_w - h$, excluding again the W windows close to the diagonal. We need to quantify the degree to which similar windows remain similar after the horizon h. To this aim, reference [7] defined the quantity

$$R_i(h) = \frac{1}{k} \sum_{l=1}^{k} g_{i+h, r_{i,l}+h}. \tag{3.17}$$

that corresponds to the mean rank (refered to the window $i + h$) of h time steps ahead of the k nearest neighbors of the window i. In case of complete predictability, the mean rank takes its smallest possible value, so we get $R_i = R_L$, where

$$R_L = \frac{k+1}{2}, \tag{3.18}$$

analogously to Eq. 2.3. For no predictability, the expected value for R_i is

$$R_i^U = \frac{M_i + 1}{2}, \tag{3.19}$$

defined analogously to Eq. 2.4. With a normalization analogous to the one of Eq. 2.2, the rank-based predictability score [7] is defined as:

$$S(h) = \frac{1}{N-h} \sum_{i=1}^{N-h} \frac{R_i^U - R_i(h)}{R_i^U - R^L}. \tag{3.20}$$

In case of complete predictability, $R_i = R^L$, therefore $S = 1$ and the expected value for no predictability is $S = 0$. These boundaries and expected values of the measure S are analogous to the ones for L (Eq. 2.2).

The predictability score $S(h)$ of Eq. 3.20 is equivalent to applying the measure L between a signal and itself shifted by the horizon h. The only

difference from our formulation of Eq. 3.14 is that for $S(h)$ we do not use circular boundary conditions: the length of the overlap between the signal and the shifted version of itself, is shorter the longer the horizon h. Accordingly, as we mentioned above, the last h windows of the signals are excluded from the analysis considering that their future is not completely present in the recorded signal.

We therefore use $S(h)$ to define *auto-L*, consistent with our previous definitions (Eqs. 3.6, 3.12, 3.13):

$$auto\text{-}L(\tau) = S(\tau), \qquad (3.21)$$

with $\tau = (1, \ldots, N_{\text{delay(auto)}}) \cdot f_{\text{shift}}$. As for *cross-L*, we choose f_{shift} always as an integer multiple of s. We call h_0 the smallest value of τ for which *auto-L*$(\tau) = 0$. This is a useful quantity because it estimates the length of the predictability interval.

3.2 Comparison for directionality detection

To compare *cross*-correlogram, *cross*-distances and *cross-L* as in Section 2.5.1, we use pairs of signals measured from unidirectionally coupled Hindmarsh-Rose dynamics, where X is the driver and Y is the response. We want to determine the direction of the coupling, assuming that we know *a priori* that if a coupling is present, it is unidirectional (the same logic as in Chapter 2). We first extract information about the time scale of the signals looking at the *auto*-functions.

We use $\Delta M_I := M_I(X|Y) - M_I(Y|X)$ to assess directionality, with the different functions $I = C, D, L$, as introduced in Eqs. 3.5, 3.11, 3.16, respectively. In particular, as in Chapter 2, we compute the values of ΔM_I for $n_r = 20$ independent realizations of the dynamics. In order to assess the significance, we perform a Wilcoxon signed rank test across the n_r realizations of the values of ΔM_I. Like in Section 2.5.1, we consider Setting A and B of the Hindmarsh-Rose dynamics, for the uncoupled case plus n_ϵ different values of the coupling. The level of significance is $\alpha = 0.05/n_\epsilon$, where we use the Bonferroni correction [114] to take into account the multiple testing of the n_ϵ values of the coupling. The performance Ψ is estimated as in Section 2.5.1 by the percentage of the n_ϵ non-zero coupling values for which we can significantly detect the coupling and its direction.

In Table 3.1 we summarize the parameters that we use for each method. We always express parameters in units of sampling time Δt, as defined in

Section 2.5.1. For the *cross*-correlogram C, we use two sets of parameters. Set 1 is a choice with small bins, no overlap between subsequent bins ($s_c = f$) and small shifts for the *cross*-correlogram. The spike train distances have no binning and no overlap; we choose f_{shift} with the same length as the step size of the *cross*-correlogram, and the same number of delays. For the measure L we use the same window length q and overlap s as in the previous Chapter 2: q (set 1) $= 1000$, s (set 1) $= 1000/5$. We also consider a different parameter choice with the same total number of windows N_w as in set 1 ($N_w = 400 \cdot 5$) but with shorter length: q (set 2) $= 1000 \cdot (2/5)$, and less overlap: s (set 2) $= 1000/2$, in order to check for the influence of those parameters on the performance, and we got similar results as for the first parameter choice (results not shown). For L the window length q is the equivalent of the bin size for C. Evidently, because of the requirements that there needs to be a certain number of spikes in each window for L, q cannot be as small as the binning of C in set 1. That is the reason why we consider the parameter set 2 for C, in which we choose the same binning as for L (set 1) and the same values of overlap.

Table 3.1: Parameters used for the comparison of the different methods, in units of sampling time Δt. The number of nearest neighbors for the measure L (Eq. 3.17) is set as $k = 5$.

method	binning	step size	f_{shift}	$N_{\text{delay(cross)}}$	$N_{\text{delay(auto)}}$
C (set 1)	$f = 20$	$s_C = 20$	1	250	1000
C (set 2)	$f = 1000$	$s_C = 1000/5$	s_C	25	100
Distances	no binning	no overlap	20	250	1000
L	$q = 1000$	$s = 1000/5$	s	25	100

3.2.1 Results

3.2.1.1 *Auto*-functions

We first show profiles of *auto*-functions to qualitatively illustrate the meaning of the parameters that we choose and compare their characteristics for different measures. In Figures 3.1 and 3.2 we depict profiles of *auto*-functions for the different methods and parameters, obtained for one realization of the driver dynamics X and different realizations of the Y dynamics, for some

Figure 3.1: Profiles of *auto*-functions for the Hindmarsh-Rose dynamics in Setting A. The first column represents *auto*-C with parameter set 1, the second column parameter set 2. The first row corresponds to one realization of the X dynamics, in this case in an irregular spiking regime. Being the driver dynamics, it does not depend on ϵ. The subsequent rows correspond to realizations of the Y dynamics, first for uncoupled dynamics ($\epsilon_0 = 0$) and then for coupled dynamics ($\epsilon_a = 0.24$). The Y signals are in an irregular bursting regime. Examples of these signals are shown in Figure 2.2. Note that for *auto*-functions with X we zoom in the x-axis in order to better resolve the oscillations of the functions.

selected values of ϵ. These values are the same as for the examples shown in Figures 2.2 and 2.3 of Chapter 2.

In general, *auto*-correlogram (set 1 and set 2) and *auto*-distance show oscillations that in many cases are consistent among these different measures for the same signals. For the irregular spiking regime (X signal in Figure 3.1) we see differences between *auto*-ISI and *auto*-SPIKE. The peaks for *auto*-SPIKE have the same frequency as the spikes: around $19/(4000 \cdot \Delta t)$ peaks in the *auto*-SPIKE profile, and this same value approximates the average number of spikes per time in the corresponding signal. The *auto*-ISI instead captures slower oscillations in rates. Another difference between *auto*-ISI and *auto*-SPIKE occurs for the almost periodic regimes ($Y(\epsilon_0)$ and $Y(\epsilon_a)$ signals in Figure 3.2). Only *auto*-SPIKE captures the frequency of the spikes, in accordance with the *auto*-correlogram (set 1). The *auto*-correlogram with the other parameter set 2 is not capturing the frequency of the almost periodic spiking, instead it is only reflecting the small variations due to the large bins with overlap ($s_C = 200$, while for set 1 $s_C = 20$). Note
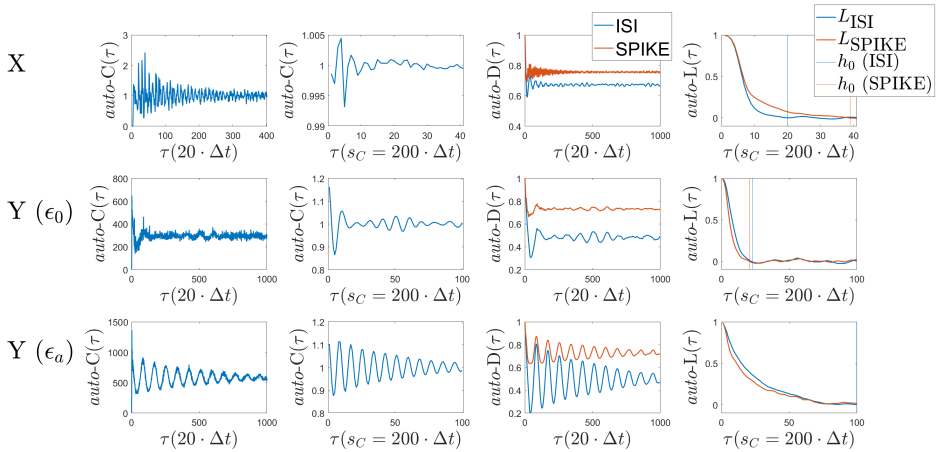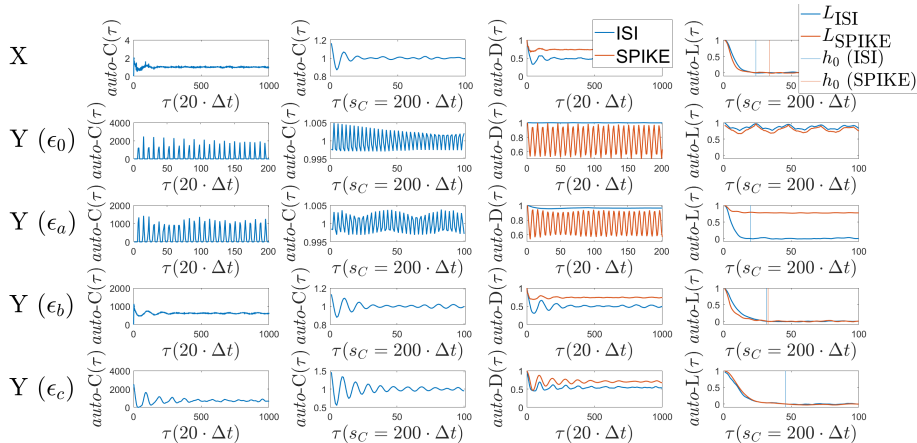
Figure 3.2: Profiles of *auto*-functions for the Hindmarsh-Rose dynamics in the Setting B. The first column represents *auto-C* with parameter set 1, the second column parameter set 2. The first row refers to one realization of the X dynamics, that is in an irregular bursting regime. The subsequent rows refer to the Y dynamics with increasing values of coupling strength. For $\epsilon_0 = 0$ and $\epsilon_a = 0.0101$ (as the example in Figure 2.3a), the signals are almost periodic. For $\epsilon_b = 0.1092$ (as Figure 2.3b) and $\epsilon_c = 1.0276$ (as Figure 2.3c), Y is an irregular bursting regime, with degeneration of bursts for the last value ϵ_c. Note that for *auto-C* (set 1) and *auto-D* with $Y(\epsilon_0)$ and $Y(\epsilon_a)$ we zoom on the x-axis for resolving the oscillations of the functions.

that a perfectly periodic function has a periodic *auto*-correlogram.

The irregular bursting regimes of the $Y(\epsilon_0)$ signal in Figure 3.1 and the X and $Y(\epsilon_b)$ signals in Figure 3.2 give similar profiles for *auto*-correlogram and *auto*-distances. In these cases, the oscillations in the profiles share the frequency of the bursts in the signals. The same happens for the more distinct bursts of the $Y(\epsilon_a)$ signal in Figure 3.1 and the $Y(\epsilon_c)$ signal in Figure 3.2. The frequency of the bursts is slightly better captured by *auto*-ISI than by *auto*-SPIKE.

Auto-L shows a different behavior since it does not oscillate. Instead it conveys straightforward information about the maximum predictability horizon h_0. We remind that τ in this case corresponds to the predictability horizon h, and h_0 is the minimum value of τ for which $S(\tau) \leq 0$. In many cases h_0 is contained within the range of τ-values that is shown, as we can see from the vertical lines in the plots of *auto-L* of Figures 3.1 and 3.2. This is reasonable considering that the interval of values of τ in the plot is the

same for which we compute the other *auto*-functions, from where we see that always many oscillations are included. The exceptions happen in the special case of almost periodic spiking ($Y(\epsilon_0)$ and $Y(\epsilon_a)$ signals in Figure 3.2). In these cases there is a very long horizon of predictability. This is due to the strong regularity in the structure of the signal, which is very close to periodicity. It is interesting to note that in the case of the $Y(\epsilon_a)$ signal in Figure 3.2, *auto-L_{ISI}* and *auto-L_{SPIKE}* are very different, evidently because the ISI and the SPIKE-distance in this regime are capturing different features of the signals. In fact, also the corresponding *auto*-ISI and *auto*-SPIKE are very different. The stronger regularity in the structure of the signal, due to the distinct bursting structures, is also responsible for the highest value of h_0 for $Y(\epsilon_a)$ in Figure 3.1.

3.2.1.2 *Cross*-functions

In Figures 3.3 and 3.4 profiles of *cross*-functions are shown for the different methods and parameters, for one realization of the driver dynamics X and different realizations of the Y dynamics, for the same selected values of ϵ as in Figures 3.1 and 3.2, respectively. We see that with *cross*-correlogram and *cross*-distances, there are oscillations in the profiles, related to the oscillations in the corresponding *auto*-functions. We remind that the difference in the maximum values of these function for negative and positive delays $M(X|Y)$ and $M(Y|X)$ is what we use for assessing directionality. From visual inspection, the profiles of *cross*-correlogram and *cross*-distances do not always look asymmetric. In the case of *cross-L* instead, the profile is always smooth (as *auto-L* of Figures 3.1 and 3.2), and clearly the peaks M_L are for small negative values of delays for both $M_L(X|Y)$ and the other direction $M_L(Y|X)$. This is a clear indication that introducing small delay helps in discriminating directionality even if the measure *L* is already directional for zero τ.

In Figures 3.5, 3.6 and 3.7 we summarize the capability of *cross-C*, *cross*-distances and *cross-L* to detect the coupling in Setting A and B of the Hindmarsh-Rose dynamics. These figures are analogous to Figures 2.4 and 2.6 in Chapter 2 [73]. In Table 3.2 we summarize the performances with the different methods.

We find that the performance of measure *L* is the best, in particular with ISI-distance. The weakest performance are obtained for *cross*-correlogram in Setting A, where it is unable to detect the coupling direction. The two parameter sets of *cross*-correlogram give similar performance, the worst

Table 3.2: Performance Ψ obtained from the comparison of the different methods. The range of values for Ψ is $0 \leq \Psi \leq 1$. For the measure L, we added in brackets the values computed in Chapter 2, with no shifts.

method	Ψ (Hindmarsh-Rose A)	Ψ (Hindmarsh-Rose B)
C (set 1)	0.14	0.35
C (set 2)	0.03	0.26
D(ISI)	0.61	0.76
D(SPIKE)	0.45	0.83
L(ISI)	0.86 (0.83)	0.91 (0.90)
L(SPIKE)	0.79 (0.72)	0.75 (0.73)
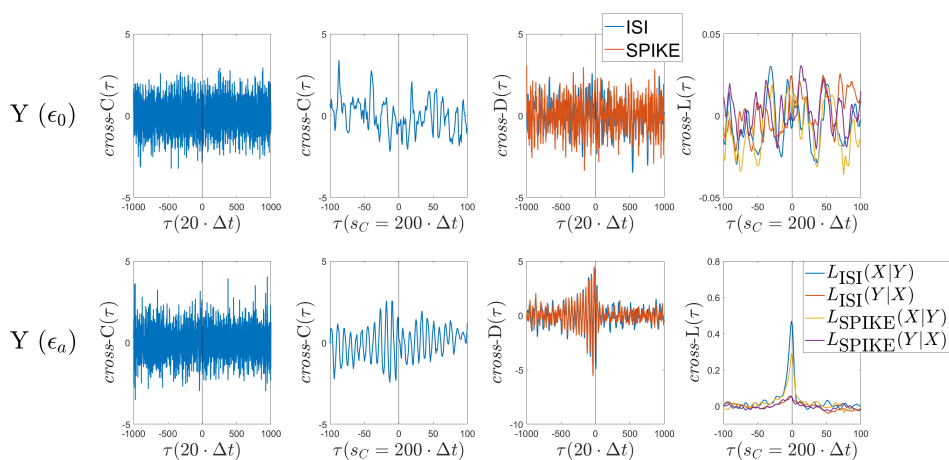
Figure 3.3: Profiles of *cross*-functions with the *standard score* normalization (Eq 3.1.1), for the Hindmarsh-Rose dynamics in the Setting A, for the same exemplary signals as in Figure 3.1. The first column represents *cross-C* with parameter set 1, the second column parameter set 2.

among the *cross*-functions. The *cross*-distances are performing better than the *cross*-correlogram, proving to be a promising approach for the detection of directionality. We note that we have no false positive detection of directional coupling: for zero coupling we never detect a significant directionality. Instead we get in one case some significant detections of the wrong direction, for some values of the generalized synchronization regime in Figure 3.5d, for M_C with parameter set 2.

The introduction of shifts improves the performance of the measure
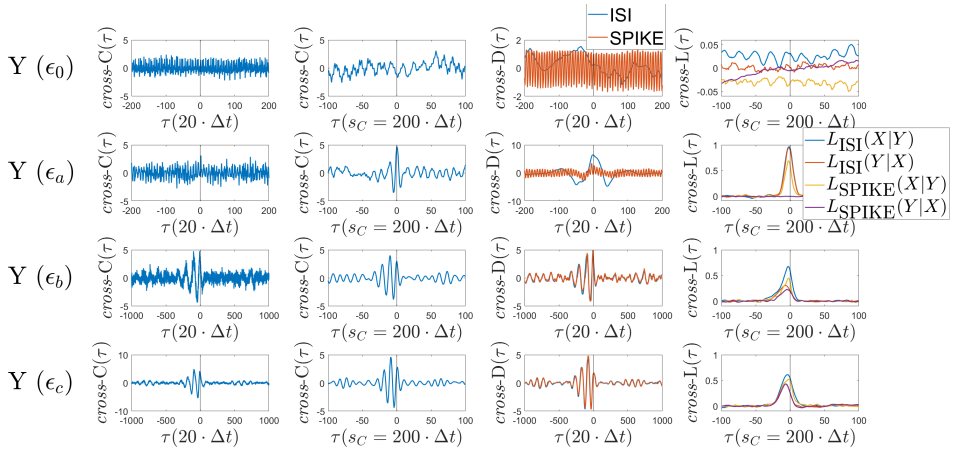
Figure 3.4: Same as Figure 3.3, but here for the Hindmarsh-Rose dynamics in the Setting B, for the exemplary signals already used in Figure 3.2.

L, as it is clear from the values of Ψ summarized in Table 3.2 (values in brackets correspond to the performances of L without shifts). We can see the improvements also by comparing Figure 3.7 with the corresponding Figures 2.4 and 2.6 in Chapter 2. We note that for the Setting B with L_{ISI} in Figure 3.7c, in contrast to the application of L at zero shift only, with *cross-L* it is possible to detect the direction of the coupling also close to the generalized synchronization regime, where the values of L are very high.

3.2.1.3 Delay values $\tau^{\max}$

In Figures 3.8, 3.9 and 3.10, we show the values of the position of the maximum $\tau^{\max}(X|Y)$, $\tau^{\max}(Y|X)$. The interval of delays that we consider is the same across the different measures, although the parameter values are different. Therefore the values of $\tau^{\max}$ can directly be compared, also visually from the plots. For the *cross*-correlogram, the delays $\tau_C^{\max}$ are spread around the whole possible interval in correspondence to the coupling values ϵ where the directionality detection fails (Figure 3.8a-b and small couplings in Figure 3.8c-d. For the Setting A of Hindmarsh-Rose, the measures that can detect directionality (spike train distances and L) share the same behavior: $\tau^{\max}(X|Y)$ attains a sharper distribution with a mean that is closer to zero, compared to the opposite direction $\tau^{\max}(Y|X)$.

High coupling values in Setting B of the Hindmarsh-Rose regime obtained in the region where all the measures detect directionality, and the
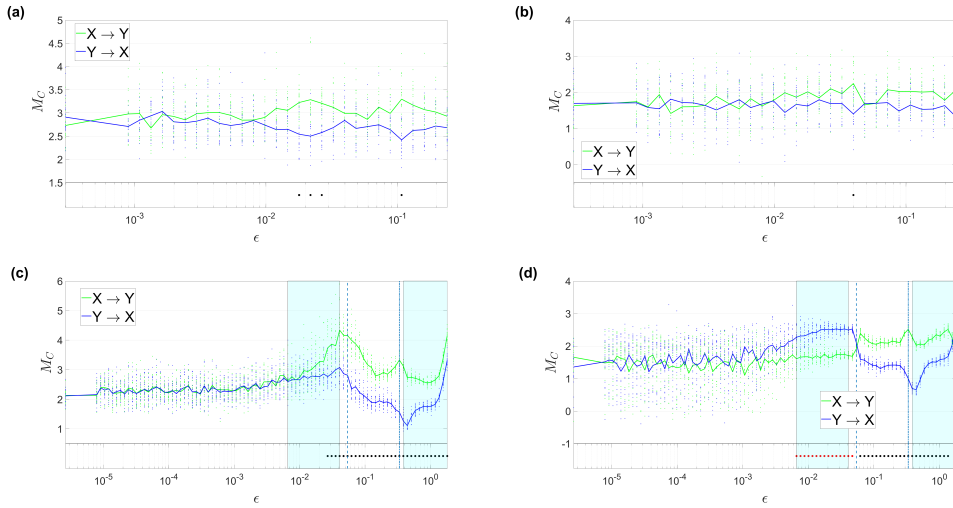
Figure 3.5: Values of M_C: $M_C(X|Y)$ and $M_C(Y|X)$, Eq. 3.5, for increasing values of the coupling strength. First row (a-b): Setting A of Hindmarsh-Rose. Second row (c-d): Setting B of Hindmarsh-Rose. On the left, parameter set 1, on the right, parameter set 2. Results for uncoupled dynamics ($\epsilon = 0$) are displayed on the ordinates. As in Figures 2.4 and 2.6, the asterisks at the bottom of the figures mark the coupling values for which there is a significant detection of the direction of the coupling, as assessed by a Wilcoxon signed rank test. As in Figure 2.6, the shaded areas in (c-d) indicate the generalized synchronization regimes. The dashed vertical line on the left distinguishes the regime close to periodicity (see Figure 2.3a) from the regime with bursts in the response (see Figure 2.3b), and the second line marks the transition to the regime for which there is a strong degeneration of the bursts (see Figure 2.3c). The black stars on the bottom of the plots mark the ϵ values for which the direction of the coupling is significantly detectable. The red stars mark the values for which the opposite direction is significantly detected. Note that in the generalized synchronization regime in (d) there are many significant detections of the wrong directionality.

qualitative agreement between the measures for the values of τ^{max} can give us information about the effect of the coupling in the Hindmarh-Rose model for that regime. Even if there is no explicit delay in the equation, because of the intrinsic dynamics of Hindmarsh-Rose model, the coupling manifests itself with an effective delay.
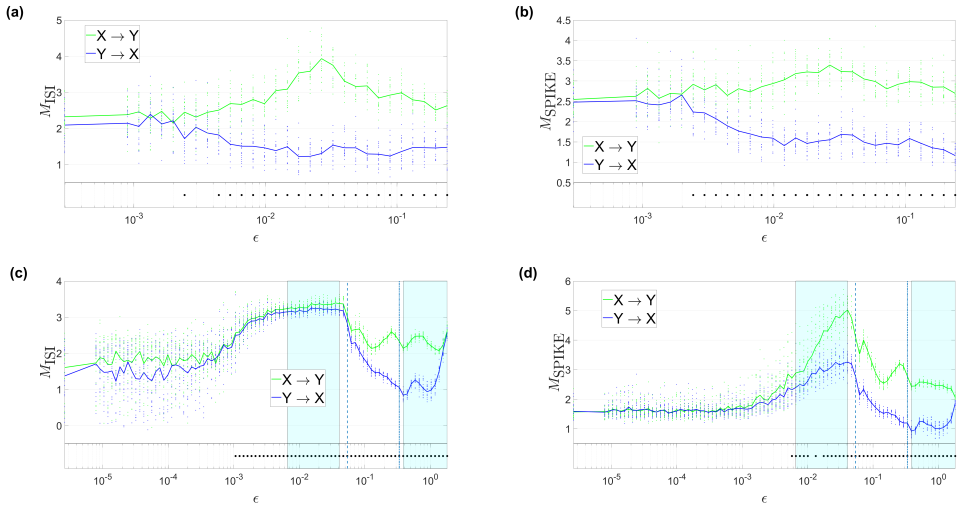
Figure 3.6: Same as Figure 3.5, but here for M_D: $M_D(X|Y)$ and $M_D(Y|X)$, Eq. 3.11. First row (a-b): Setting A of Hindmarsh-Rose. Second row (c-d): Setting B of Hindmarsh-Rose. On the left, results for ISI-distance, on the right, SPIKE-distance.
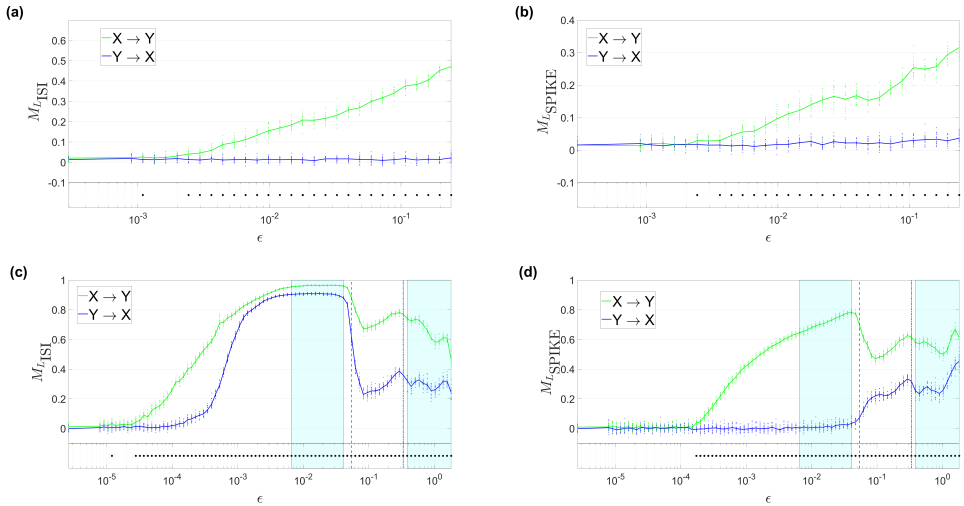
Figure 3.7: Same as Figures 3.5 and 3.6, but here for $M_L(X|Y)$: $M_L(X|Y)$ and $M_L(Y|X)$, Eq. 3.16. First row (a-b): Setting A of Hindmarsh-Rose. Second row (c-d): Setting B of Hindmarsh-Rose. On the left, results for L_{ISI}, on the right, L_{SPIKE}. These figures are analogous to those of Figures 2.4 and 2.6 of Chapter 2, with the difference that here we plot M_L instead of L.
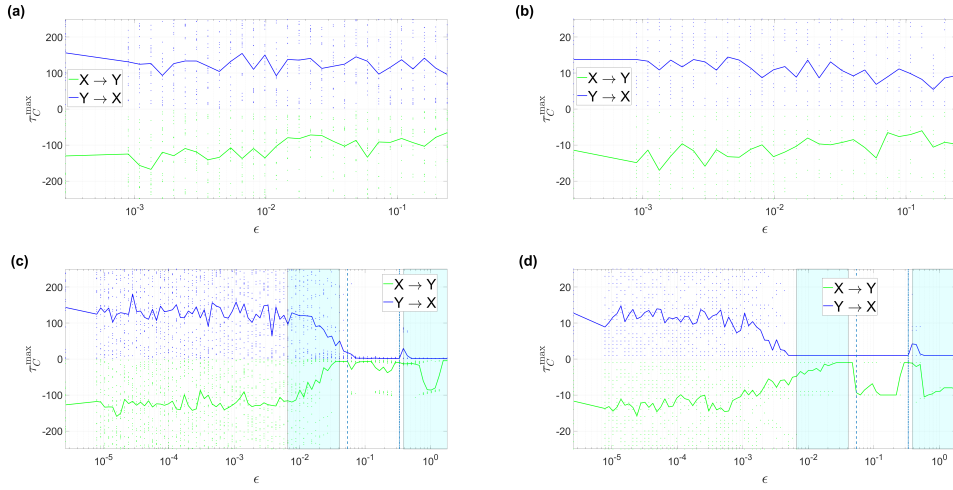
Figure 3.8: Values of $\tau_C^{\max}(X|Y)$ and $\tau_C^{\max}(Y|X)$ corresponding to the results of Figure 3.5. The two continuous curves are the average of $\tau_C^{\max}$ across n_r realizations for each coupling value. The vertical lines and shaded areas have the same meaning as in Figure 3.5.
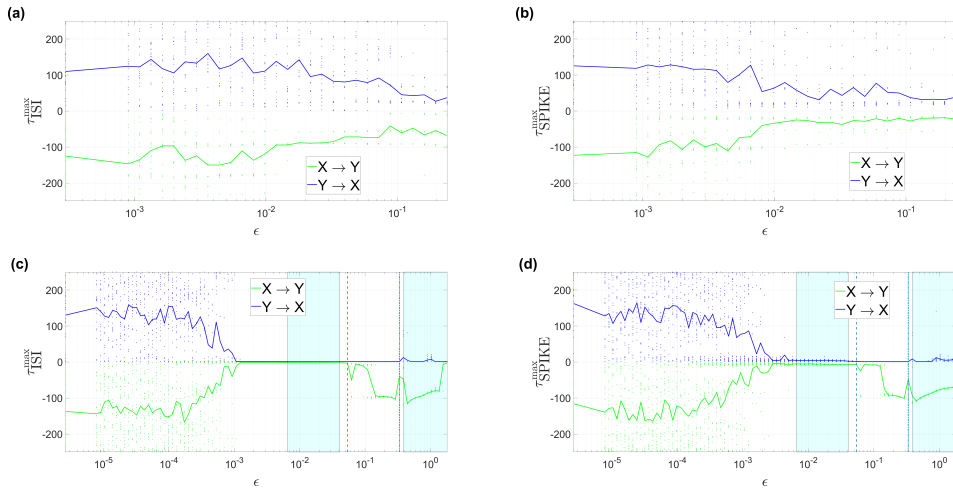
Figure 3.9: Values of $\tau_D^{\max}(X|Y)$ and $\tau_D^{\max}(Y|X)$ corresponding to the results of Figure 3.6.
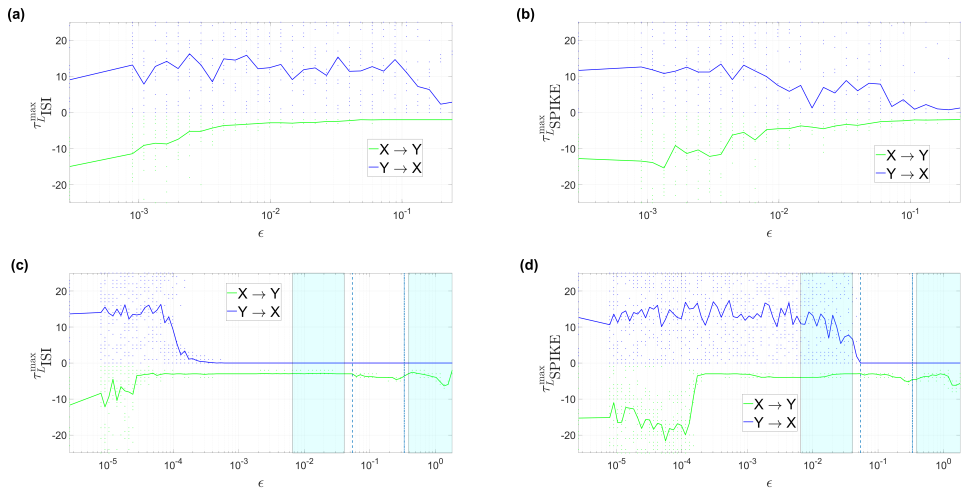
Figure 3.10: Values of $\tau_L^{\max}(X|Y)$ and $\tau_L^{\max}(Y|X)$ corresponding to the results of Figure 3.7. Note that here also zero is a possible value for τ.

3.3 Comparison using surrogate techniques

In the last Section we used different methods to detect directionality between two signals. We assumed to know that if a coupling is present, it is unidirectional. Furthermore, we took advantage of the fact that we are working with simulated data to generate a distribution of $n_r = 20$ realizations for each coupling value ϵ. We used the statistical difference between the distributions of values of a measure for assessing the directionality. In this Section we change the perspective. We continue to further approach settings and conditions that we encounter when dealing with real data. At the same time, we are interested in comparing the measures also from the general point of view of interdependence detection, regardless of directionality. Accordingly, we do not assume to know *a priori* if the coupling is unidirectional, but more importantly, we do not use a distribution of values obtained from many realizations. The common approach to measure interdependence with these conditions is to compute surrogates.

Surrogates allow one to test a well-defined null hypotheses H_0 about the dynamics underlying some experimental data [5]. They are signals derived from the original signals under study, and depending on the null hypothesis they maintain only certain properties of the original signals while all other properties are destroyed. In our study, we want to test the null hypothesis that the signals are independent. Otherwise, we make no further assumptions. Accordingly, we ideally want to maintain all the properties except those that have to do with interdependence or correlation: the auto-correlogram, the distribution of intervals between subsequent spikes, the nonstationarity in rate. The best way to do that are time shifts between the two signals. Therefore, we calculate the measures not only for the original signals but also for an ensemble of surrogates, each computed with a different time shift between the original signals. If we find a significant difference in the coupling estimation between real signals and surrogates, we can reject the hypothesis H_0 that the original signals are independent. The *cross*-functions are the values of the measures obtained for these surrogates. We use the same *cross*-functions introduced before, but now the time shifts are not 'small', but instead they need to be sufficiently large in order to guarantee the independence between the original signal and its shifted version.

We here adapt the notation for describing the *cross*-functions. In this case we always use the circular boundary condition because the shift is higher. For the *cross*-correlogram we use a formulation similar to Eq. 3.1,

but here with circular boundary conditions $x_{\text{count}}(-t_C) = x_{\text{count}}(Q - t_C)$, and the same for $y_{\text{count}}(t_C)$:

$$cross_S\text{-}C(\tau) = \sum_{t_C=0}^{Q} x_{\text{count}}(t_C) \cdot y_{\text{count}}(t_C - \tau), \tag{3.22}$$

with $\tau = (-N^S_{delay(cross)}, \ldots, N^S_{delay(cross)}) \cdot f^S_{\text{shift}}$. The $cross_S\text{-}ISI(\tau)$ and $cross_S\text{-}SPIKE(\tau)$ are defined in Eqs. 3.7 and 3.8, with $\tau = (-N^S_{delay(cross)}, \ldots, N^S_{delay(cross)}) \cdot f^S_{\text{shift}}$, but as a consequence of circular boundary conditions, the distances are computed for the time range $t = 0, \ldots, Q$. The definition of $cross_S\text{-}L(X|Y)(\tau)$ is the same as in Eq. 3.14.

We want to use a f^S_{shift} long enough that we can assume that $x(t)$ and $y(t + f^S_{\text{shift}})$ are independent, and also the surrogate values for different shifts are independent among them. We therefore take the following approach. We fix the total number of surrogates ($N^S_{delay(cross)} = 20$) and we take the longest interval for f^S_{shift} that allows to have $N^S_{delay(cross)}$ non-overlapping surrogates equidistantly distributed. In Table 3.3 we summarize the parameters that we use. The choice of the binning is the same as in Table 3.1 from the previous Section 3.2.

Table 3.3: Parameters used for the comparison of the different methods using the surrogates, in units of sampling time Δt. Note that the binning is the same as in Section 3.2, while f_{shift} is just slightly shorter than the interval covered by the *auto*-functions (see parameters in Table 3.1). The value of $N^S_{delay(cross)}$ is $N^S_{delay(cross)} = 20$. The number of nearest neighbors for the measure L (Eq. 3.17) is set as $k = 5$.

method	binning	step size	f^S_{shift}
C (set 1)	$f = 20$	$s_C = 20$	$19 \cdot 1000$
C (set 2)	$f = 1000$	$s_C = 1000/5$	$19 \cdot 5$
Distances	no binning	no overlap	$19 \cdot 1000$
L	$q = 1000$	$s = 1000/5$	$19 \cdot 5$

If the assumption that surrogates are independent holds, we can compute the *standard score* to assess the significance of the value of the *cross*-function at zero shift:

$$Z_C := \frac{cross_S\text{-}C(0) - \text{mean}(cross_S\text{-}C)}{\text{std}(cross_S\text{-}C)}, \tag{3.23}$$

where the mean mean($cross_S$-C) and the standard deviation std($cross_S$-C) are taken across the $N_{delay(cross)}^S$ shifts. For the distances and the measure L we analogously get Z_D (Z_{ISI}, Z_{SPIKE}) and Z_L ($Z_{L_{ISI}}$ and $Z_{L_{SPIKE}}$).

In cases when $Z > Z_{thr}(\alpha_S)$, for a single realization, the null hypothesis of independence between the signals can be rejected at a significance level of $\alpha_S = 0.05/n_\epsilon$, where we use the Bonferroni correction [114] to take into account the multiple testing of the n_ϵ values of the coupling.

Here we consider the same Settings A and B of the Hindmarsh-Rose dynamics as in Section 3.2, with only $n_r = 1$ realization for each coupling value. We then compute Z values for each realization, from the $cross_S$ functions for $N_{delay(cross)}^S$ surrogates. In order to evaluate the performance of the surrogates approach to assess the presence of the coupling, we compute Ψ_S which is defined as the percentage of non-zero coupling values for which $Z > Z_{thr}(\alpha_S)$.

To verify if the null hypothesis of independence holds between $x(t)$ and $y(t + f_{shift}^S)$, and between all the pairs of signals at different shifts, we look at the profile of *auto*-functions (Figure 3.1 and 3.2). These functions contain information about the length of the interval that guarantees that the signal loses the memory about its past. We can see that the oscillations of *auto-C* and *auto-D* are damped for $\tau = f_{shift}^S$. Also *auto-L* goes to zero even for smaller values of τ, meaning that the horizon of predictability h_0 is $h_0 < f_{shift}^S$. The only exceptions occur in the range of coupling values for which the Y dynamics is in an almost periodic regime ($Y(\epsilon_0)$ and $Y(\epsilon_a)$ of Figure 3.2). These are special cases because periodicity strongly affects *auto*-functions.

3.3.1 Results

In Figures 3.11 and 3.12 (equivalent to Figures 3.3 and 3.4) we show profiles of $cross_S$ -functions for the different methods and parameters, for one realization of the driver dynamics X and different realizations of the Y dynamics, for some selected values of ϵ. We can see that the values at different delays look independent. Note that for $cross_S$-D in Figure 3.11 there are negative peaks at zero delay. This shows that in some cases the coupling could be detected not only by a high level of similarity for no shift between the signals, but also by a high level of dissimilarity.

In Figures 3.13, 3.14, 3.15 we show the capability of Z_C, Z_D and Z_L to assess the interdependence between the X and Y dynamics for Setting A and B of the Hindmarsh-Rose neurons. The corresponding values of the
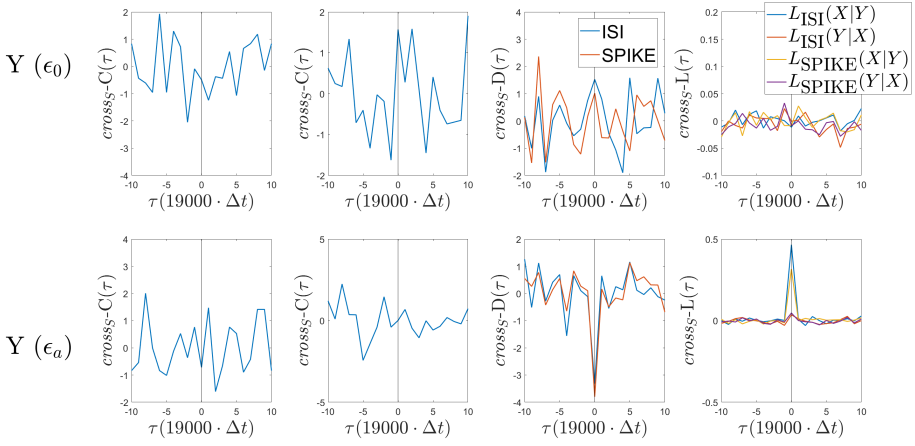
Figure 3.11: Profiles of *cross_S*-functions for surrogates for the Hindmarsh-Rose dynamics in the Setting A, for the same exemplary signals as in Figure 3.1. The first column represents *cross_S-C* with parameter set 1, the second column parameter set 2. For *cross_S-C* and *cross_S-D* we show *standard score* (Eq. 3.1.1) as normalization to the functions. Note that for *cross_S-D* there are negative peaks at zero delay. The smallest values are obtained for *cross_S*-SPIKE.
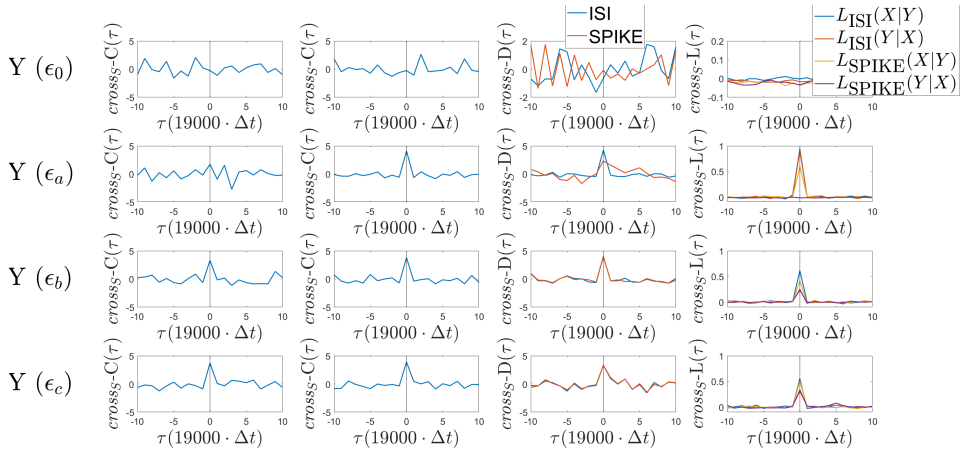
Figure 3.12: Profiles of *cross_S*-functions for surrogates for the Hindmarsh-Rose dynamics in the Setting B, for the same exemplary signals as in Figure 3.2. The first column represents *cross_S-C* with parameter set 1, the second column parameter set 2.
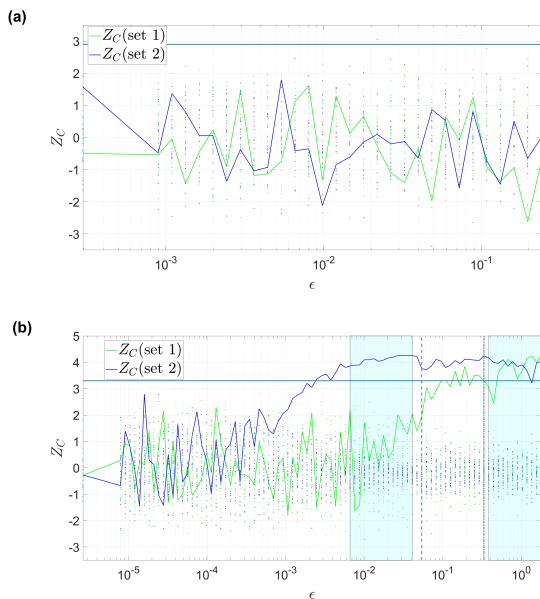
Figure 3.13: Values of Z_C for increasing values of the coupling strength (for the two parameter sets). The points are the values of the surrogates. (a): Setting A of Hindmarsh-Rose. (b): Setting B of Hindmarsh-Rose. Results for uncoupled dynamics ($\epsilon = 0$) are displayed on the ordinates. The horizontal lines represent the threshold value of $Z_{thr}(\alpha_S)$, with $\alpha_S = 0.05/n_\epsilon$. For the Setting A, $n_\epsilon = 29$ and $Z_{thr}(\alpha_S) \approx 2.9$, while for the Setting B, $n_\epsilon = 89$ and $Z_{thr}(\alpha_S) \approx 3.3$.

Table 3.4: Performance Ψ_S obtained from the different methods with surrogates. The range of values for Ψ is $0 \leq \Psi \leq 1$. We compare them with the values of Table 3.2. For the measure L we compute Ψ_S not only for the relevant direction of the coupling $X \to Y$ but also for the opposite direction $Y \to X$.

method	Ψ_S (Hindmarsh-Rose A)	Ψ_S (Hindmarsh-Rose B)
C (set 1)	0	0.18
C (set 2)	0	0.53
D(ISI)	0	0.61
D(SPIKE)	0	0.33
L(ISI)$(X\|Y)$	0.72	0.85
L(ISI)$(Y\|X)$	0	0.73
L(SPIKE)$(X\|Y)$	0.59	0.71
L(SPIKE)$(Y\|X)$	0.03	0.30
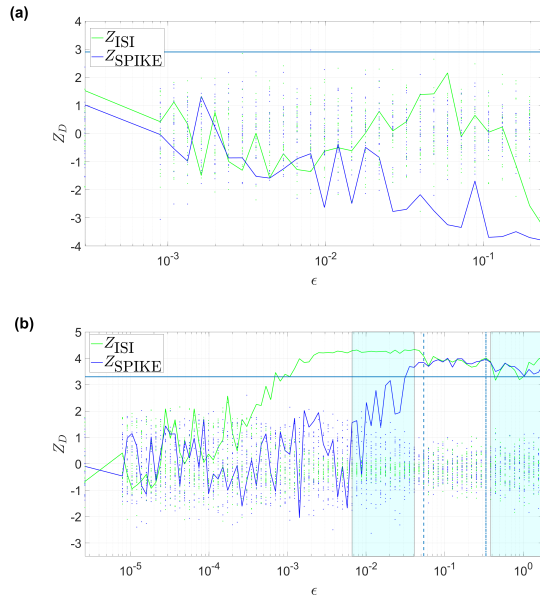
Figure 3.14: Same as Figure 3.13 but here for Z_D (Z_{ISI}, Z_{SPIKE}) for increasing values of the coupling strength. Note that in (a) with Z_{SPIKE} there are significantly negative values, meaning that $x(t)$ and $y(t)$ are more dissimilar than the average values at different delays, as we can see also from the exemplary profiles of $cross_S(D)$ in Figure 3.11.

performance Ψ_S are summarized in Table 3.4. We can see that, as in the comparison of the previous Section 3.2, the measure L performs best also in this case, with L_{ISI} giving the best performance overall. In Setting A, only L can detect the coupling. Furthermore, the values in the opposite direction $Z_L(Y|X)$ are never significant (with only one coupling value as exception). This means that we can fully reconstruct the presence and direction of the coupling with only one realization, as in the real data scenario, while the linear methods cannot detect any couplings.

In Setting B, performances Ψ_S are better with all the methods, as compared to Setting A. We should note that the values of $Z_L(Y|X)$ are now more often significant as well. Therefore, an evaluation of the directionality for these cases needs to be based on the comparison of the coupling strengths in the two directions and consequent assessment of the main direction. Overall, the performances Ψ_S are generally not as good as the performances Ψ of Section 3.2. Nevertheless, we remind that here we have only one realization for each coupling value, therefore we are considering a much harder and

53
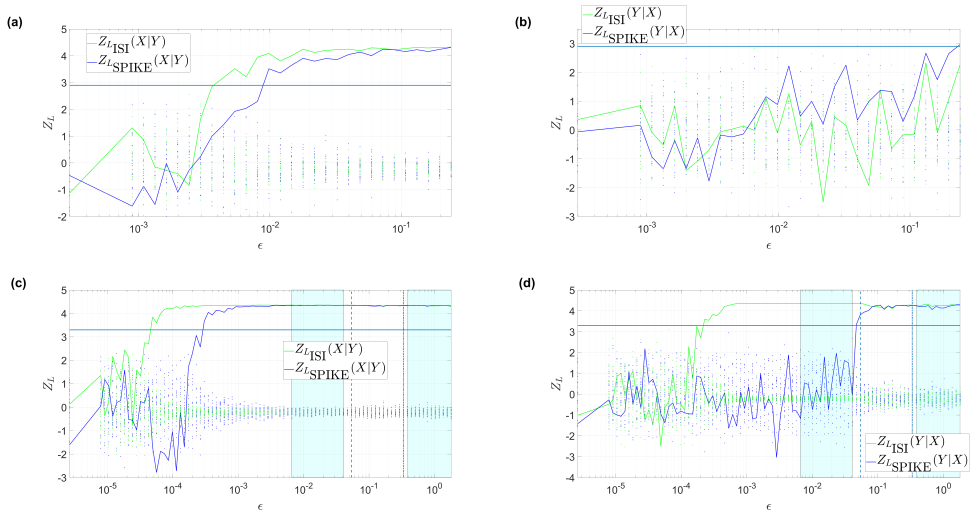
Figure 3.15: Values of Z_L ($Z_{L_{\text{ISI}}}$ and $Z_{L_{\text{SPIKE}}}$) for increasing values of the coupling strength. (a-b): Setting A of Hindmarsh-Rose. (c-d): Setting B of Hindmarsh-Rose. Figures (a) and (c) are the equivalent of Figures 3.13 and 3.14 but for $Z_L(X|Y)$, while in (b) and (d) we show the values of $Z_L(Y|X)$, correspondent to the opposite direction of the coupling.

more realistic approach.

The spike train distances, that in Section 3.2 proved to be good in detecting directionality, are suited also for detecting interdependence with surrogates, but are not sensitive to small couplings and we show that there are regimes where they cannot detect directionality. Setting A of the Hindmarsh-Rose dynamics with the SPIKE distance (Figure 3.14a) is a quite special case. In fact, the performance of Z_{SPIKE} is zero in the way we compute it, but for high coupling values Z_{SPIKE} obtaines values significantly negative, meaning that the two signals $x(t)$ and $y(t)$ at zero delays are more dissimilar than when they are shifted. Therefore, it is possible to also use dissimilarity for coupling detection.

3.4 Discussion

Among the different measures, the measure L proves to be the most sensitive measure for coupling detection. We first compare the capability of assessing directionality (Section 3.2) using $n_r = 20$ realizations of the dynamics for each coupling value, a scenario that helps us to test the approaches but that

would not be directly applicable to real data, where normally we have only one realization. Then we introduce the surrogates for simulating the study of real data (Section 3.3). The measure L gives excellent results in both cases. In particular, in Setting A of the Hindmarsh-Rose dynamics, the correlogram and the spike train distances almost cannot detect directionality, while the measure L is sensitive also to small coupling values.

In this Chapter we use for the first time spike train distances for directional coupling detection. We show that they perform generally better than the other linear measure, the *cross*-correlogram. Moreover, the adaptive properties of the measure based on spike train distances considerably decrease the choice of parameters that we need to make, and this can be very useful. However, spike train distances are not always capable to detect couplings, and furthermore, we found examples in which they detect the wrong directionality.

We show examples of *auto*-functions to illustrate the differences when they are computed with different methods. *Auto*-correlogram and *auto*-distance give important information regarding the frequencies in the signals, in dependence on the binning, the shift and the distance that we use. This information is overall quite consistent between the different measures. In the case of the *auto-L* (or predictability) we have a smooth profile, as for *cross-L* which does not contain any information about the frequencies. It instead provides straightforwardly the values of the predictability horizon h_0 that is the important quantity for our aim, because it estimates the time scale that we are interested in for the scope of surrogates computation, i.e. a temporal horizon wherein different states are strongly related to each other.

The value h_0 may be too large to allow the computation of a sufficient number of surrogates. The interval can be too long for different reasons. In the examples of this Chapter, it was due to the regularity of the signals. Another characteristic of the data that could induce high value of h_0 could be nonstationarity. A strong nonstationarity would at the same time influence the value of h_0 and also bias the estimation of coupling with the measure L.

A crucial aspect of this Chapter is the comparison between linear and nonlinear measures. In particular, *cross*-correlogram with parameter set 2 is looking at the same binning etc., as the measure L. We show how much more sensitive is the nonlinear measure L for coupling detection, even when it looks at the same time scale. The advantage of the measure L comes from the asymmetric state similarity criterion (Section 2.1). The information about the coupling is extracted by the comparison between similarity of different windows of one signal with different windows of the other signal.

The criterion can in fact be applied also between a point process and a continuous signal [6], thanks to this property. As we learn from the study of chaotic dynamics, the property is useful to detect small couplings, when we are dealing with dynamical systems [18]. It is interesting to make the same comparison also in the context of neuronal data. Real data have a more irregular structure compared to simulated Hindmarsh-Rose data, and in this case it is not so clear how much more information can be extracted with nonlinear approaches. On the other hand, the measure L is evidently more complex and computationally demanding than the linear measures. In the next Chapter we will apply the measures on real data to show complications that can arise. Again, we will also compare the different approaches.

Interaction between single neurons in different brain regions

In the previous chapters we extensively tested the performance of the nonlinear measure *L*, and we compared it with the linear measures *cross-correlogram* and spike train distances. Here we apply all measures tested in Chapter 3 to spike trains signals from the human brain. In this case we are dealing with multiple signals and not just single pairs. Nevertheless, the techniques that we apply are still bivariate, and aim at studying functional connectivity between the single neurons [33]. Accordingly, if we detect coupling between two units, this does not necessarily imply a physical connection between them, instead it is just an interdependence relation. This means that the neurons can for example interact through a third unit (that may be one of the measured units or not) or they can be driven by a common input.

4.1 Dataset description: Single unit recordings from an epilepsy patient

The dataset is composed by data of one night recording from one epilepsy patient suffering from pharmacologically intractable epilepsy. He was implanted with depth electrodes for intracerebral electroencephalographic

monitoring to localize the epileptogenic focus. Electrode locations were defined exclusively by clinical criteria. From the tip of each depth electrode a bundle of nine micro-electrodes sticked out. For the description of the experimental setting, please refer to [82]. Recordings were made in the following regions: amygdala (A), parahippocampal cortex (PHC), entorhinal cortex (EC), posterior hippocampus (PH), middle hippocampus (MH), anterior hippocampus (AH).

For our analysis, we use temporal windows of length $T = 20$ minutes. The classification in the dataset is: awake, sleep stage 1, 2, 3 and REM. We are interested in epochs all in the same state, i.e. awake or in a particular sleep stage. We merge sleep stage 2 and 3 together and we refer to this joint state as slow wave sleep (SWS). With this classification, we have 6 windows of *awake* (*w*) and 4 of SWS, while we do not have sleep stage 1 and REM. The sequence of sleep stage is: *w*/*w*/*w*/SWS/SWS/*w*/*w*/SWS/SWS/*w*/*w* (eleven temporal windows). The regions are A, AH, EC, MH, PHC in the left hemisphere, A, AH, MH in the right hemisphere. Note that the electrodes are in different regions in the different hemispheres. The spike trains are obtained with spike sorting [82] from the local field potential recorded by the electrodes. Each spike train corresponds to one unit, that can likely represents one or more neurons (i.e. single or multi-unit). We do not make distinctions between these two cases in our analysis. In our dataset we had 65 signals in the right hemisphere, 58 in the left. For the following analysis we select only signals that have more than 500 spikes in each 20 minutes window. There are in total $N_{\text{unit}} = 35$ units in the left hemisphere, and $N_{\text{unit}} = 30$ units in the right hemisphere, that fulfill the requirements.

4.2 Estimation of connectivity with linear and nonlinear methods

We apply again the methods described in Chapter 3. In particular, we compute *cross*-functions (Sections 3.1.1, 3.1.2 and 3.1.3), and also *cross*-functions as surrogates (Section 3.3). In Table 4.1 we summarize the parameters. Regarding the precision of the signals, here 1 ms corresponds to the smallest bin of the previous Chapters 2 and 3, but here the signals are longer, $Q = 12 \cdot 10^5$ ms ($= 20$ minutes). As a consequence, for the measure L we fix $N_w = 400$ and we get $q = 3000$ ms. The parameters of the other measures

Table 4.1: Parameters used for the comparison of the different methods, in units of ms (corresponding to the sampling time). We use $N^S_{delay(cross)} = 20$. The number of nearest neighbors for the measure L (Eq. 3.17) is set as $k = 5$.

method	binning	step size	f_{shift}	$N_{\text{delay(cross)}}$	f^S_{shift}
C (set 1)	$f = 60$	$s_C = 60$	1	150	$59 \cdot 1000$
C (set 2)	$f = 3000$	$s_C = 3000/5$	s_C	15	$19 \cdot 5$
distances	no	no	60	150	$59 \cdot 1000$
L	$q = 3000$	$s = 3000/5$	s	15	$19 \cdot 5$

are updated accordingly. We reconstruct the connectivity separately in each hemisphere. We only take into account connections which are classified as significant by our surrogate test, with a threshold of $\text{thr}_S = 3$. For the unit neurons that we consider to be connected, we then estimate directionality of the coupling from the *cross*-functions: We compute $M_C(i|j)$, $M_D(i|j)$ and $M_L(i|j)$, between all the pairs of neurons $i, j = 1, \ldots N_{\text{unit}}$.

We call W the matrix of connectivity estimation:

$$W(i, j) = \begin{cases} 0, & \text{if } Z(i, j) < \text{thr}_S \\ M(i|j) - M(j|i), & \text{otherwise.} \end{cases} \tag{4.1}$$

We make the matrices antisymmetric by using the difference $M(i|j) - M(j|i)$.

4.3 Results

Table 4.2: Fraction of significant connections over the possible number of connections, within the same region and across different regions, in the awake and slow wave sleep stage.

method	w same	w different	SWS same	SWS different
C (set 1)	0.350	0.024	0.822	0.142
C (set 2)	0.107	0.007	0.389	0.087
D(ISI)	0.124	0.006	0.633	0.143
D(SPIKE)	0.255	0.014	0.850	0.220
L (ISI)	0.028	0.001	0.118	0.034
L (SPIKE)	0.046	0.002	0.110	0.037

In Figures 4.1, 4.2, 4.3 and 4.4 we show examples of reconstruction W obtained with different methods. Note that the positive values correspond to the most driving unit and the negative to the most driven. In Table 4.2 we summarize the proportion of significant connections that we find with the different methods, separately for the connections within the same region and between different regions, during the awake or slow wave sleep stage. A value of 1 would mean that all the units are connected with all the others.

All the methods that we use detect significant couplings in spike trains recorded from the brain of epilepsy patients. This holds true not only between units in the same brain regions, but also between units in different regions. As expected, there are more significant connections within the same regions. Furthermore, we found generally more connections in the slow wave sleep stages. In these stages there are many more connections also between different regions. In the awake states instead, we detect very few connections between different regions. For the left hemisphere of the patient, we find many connections particularly between amygdala (A) and entorhinal cortex (EC).

Overall, linear measures find more significant connections than the nonlinear measure L. This holds true also if we consider the *cross*-correlogram with the parameter set 2, that uses exactly the same binning as the measure L. In Chapter 3 we showed that the nonlinear measure L is more sensitive to small coupling values than the linear measures. In contrast, in this Chapter we find more significant connections with linear measures. This is an indication that in this dataset the interdependence between units can be described in terms of correlated spike timings between units, at time scales of dozens of ms. In fact, the methods that find more connections are C (set 1) and SPIKE train distance, that both focus on spike timing at small time scales. ISI distance that focuses more on rate indeed finds less connections, and the same holds for C (set 2), that averages longer time scale as L.

4.4   Discussion

We find stable patterns in the reconstructed connectivity across the different epochs of 20 minutes in the same stage. Pronounced differences are found when we compare results from the awake state against those from the slow wave sleep. Connectivity patterns during slow wave sleep are more stable.

These effects can be explained by the different statistics of the spike trains during slow wave sleep. This stage is characterized by slow oscillations between up and down states in cortical neurons [84]. Synchronous oscillations can be both a local or global phenomenon, with most of the sleep slow waves occuring locally and also propagating between different brain regions [84]. This mechanism is thought to be key to maintain network statistics that promote skewed distributions of neuronal firing rate, promoting at the same time the integration of new memory traces [67]. Taking these studies into account, it is not surprising that we found more connections during SWS, and in particular between different areas. In a similar study [88], Olcese et al. applied nonlinear information theoretical measures of functional connectivity to single-cell recordings in the neocortex and hippocampus of rat, during both awakefulness and sleep. They found that during non-REM sleep there was a decrease in coupling between excitatory neurons located in distinct brain areas, while local and long-range coupling between interneurons were preserved. Since these recordings were performed in rats, it was easier to perform them under controlled conditions as compared to our recording from an epilepsy patient. These controlled conditions allow one to better validate the results obtained from these recordings. In future studies it can therefore be interesting to apply the nonlinear measure L for the same dataset to compare the information that can be extracted.

We show results for one patient but we found similar results for other patients as well. However, we chose to show only this example because the variability in the settings only adds complexity to the descriptions. We make here a first step in the analysis of coupling between single neurons in different regions of human brain. The capability of reliably detecting different kinds of connectivity between single neurons is a challenging problem in neuroscience research. From single-unit neuronal recordings outstanding discoveries were made [63, 101]. From similar recordings of cellular activity in vivo during seizure onsets the local origin of the seizures have been studied [110, 116] and also the burst firing changes of neurons before the seizure [35]. These studies were made during the transition to seizures (and in some temporal interval before and after the seizure), while in our dataset seizures are not present. If we better understand the interplay between different brain regions in dependence on different sleep stages, this could be a further step to understand how memory works at single neurons level [36]. We here show the potential and the caveats in the application of data analysis techniques. The analysis of bigger datasets is necessary to further substantiate our preliminary conclusions, and extend the precious

knowledge that this unique dataset can provide.
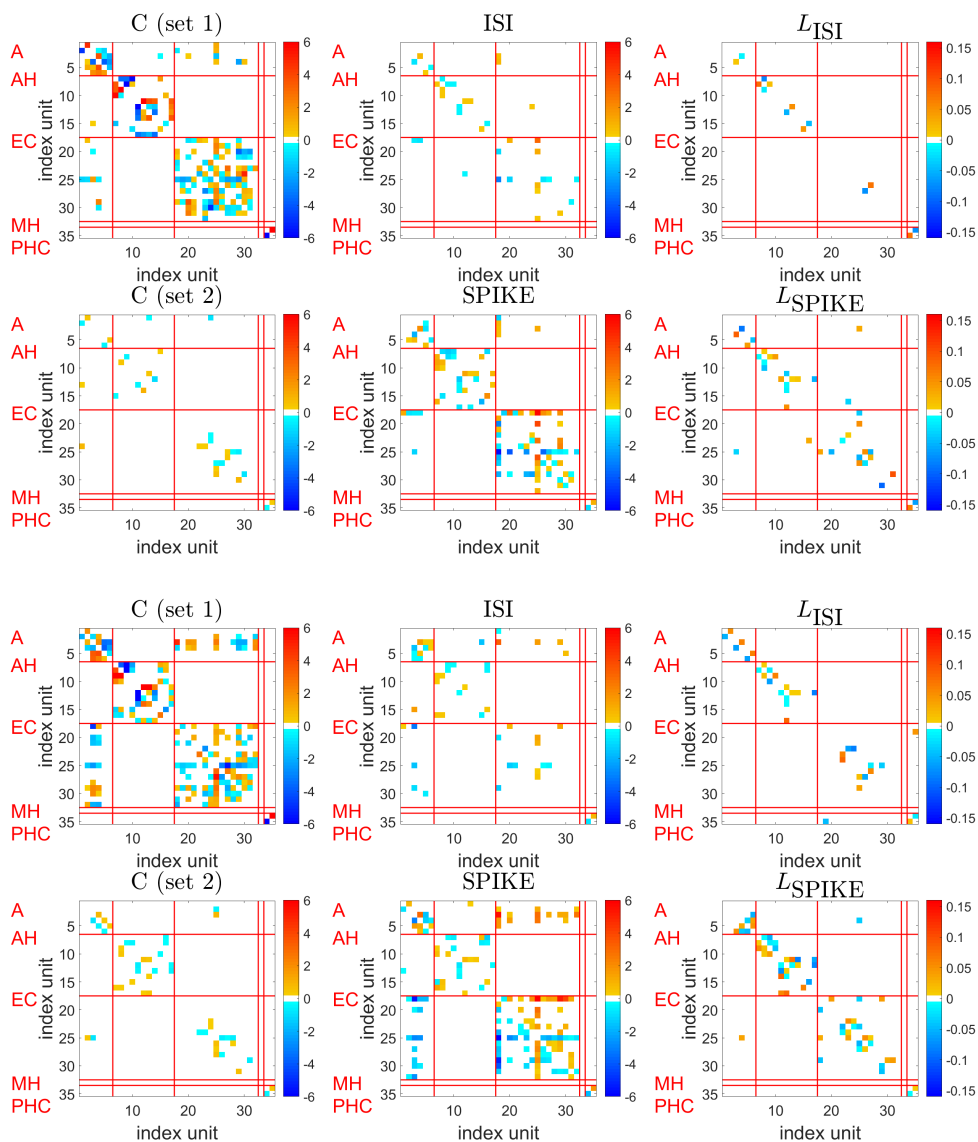
Figure 4.1: Matrix of connectivity estimation W for the left hemisphere in two different windows in the awake state (top six and bottom six matrices). Each matrix is computed with a different methods (C(set1), C(set2), D(ISI), D(SPIKE), L_{ISI}, L_{SPIKE}). The group of units delimited by red lines correspond to the different brain regions: A, AH, EC, MH, PHC. White color indicates connections that are not significant, the reddish colors indicate mainly driving units, while the bluish mainly driven.
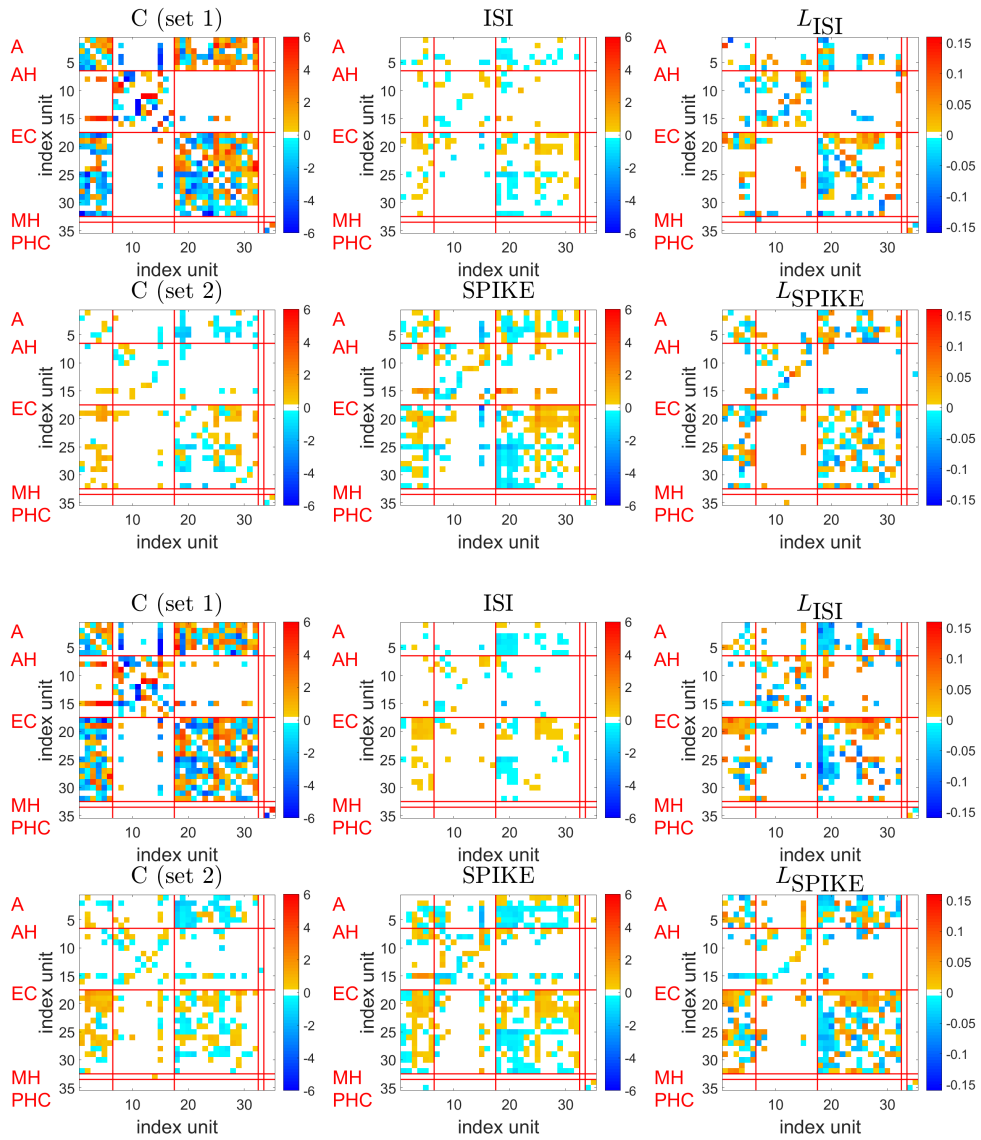
Figure 4.2: Same as Figure 4.1 but here for two windows recorded during the slow wave sleep stage.
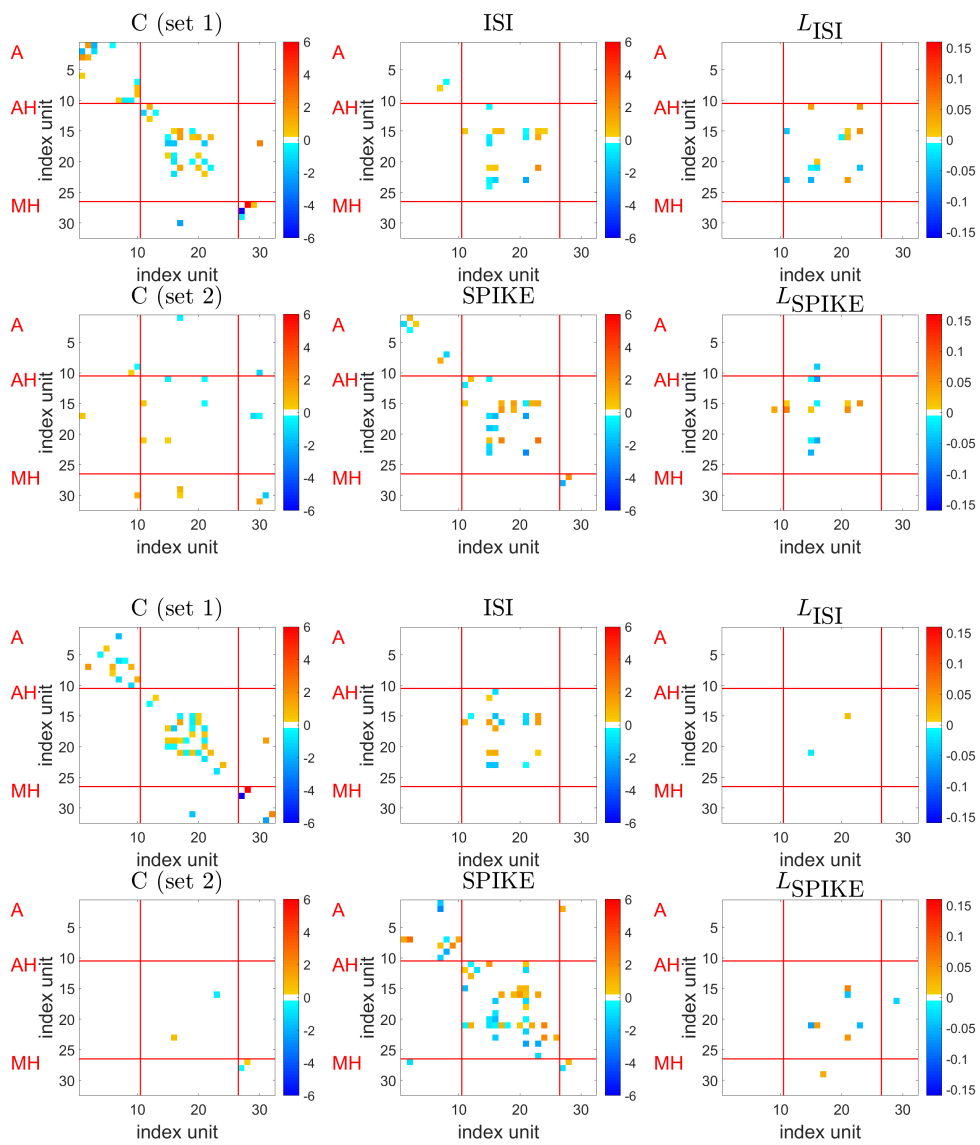
Figure 4.3: Same as Figure 4.1, 4.2 but here for the right hemisphere in two windows recorded during the awake state.
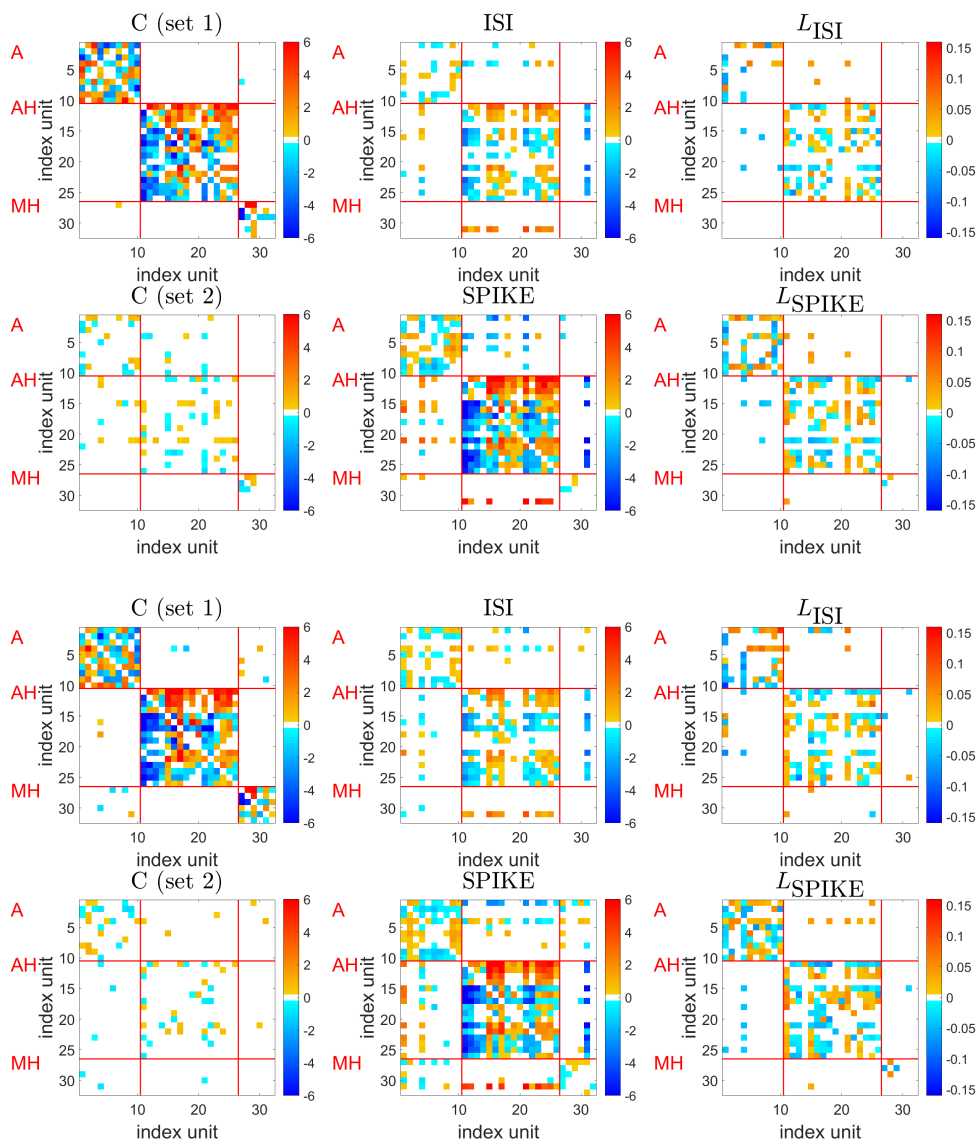
Figure 4.4: Same as Figure 4.1, 4.2, 4.3 but here for the right hemisphere in two windows recorded during the slow wave sleep stage.

CHAPTER 5

Conclusion

In this thesis we tested the performance of the nonlinear measure L with different settings of Hindmarsh-Rose dynamics. We proved its robustness to noise, and we showed that L with ISI- and SPIKE-distance provides complementary information (Chapter 2). Moreover, L can be applied to analyze spike trains from different regimes of the Hindmarsh-Rose dynamics, such as irregular spiking, irregular bursting, generalized synchronization. We furthermore introduced time shifts between pairs of spike trains. These shifts can be used in two different ways. On the one hand, they allow one for the detection of delay in the coupling. On the other hand, they can be applied to construct surrogates. With this framework we compared the performance of L against the cross-correlogram and the spike train distances. For coupled Hindmarsh-Rose neurons, the measure L proved to be the best approach for estimating coupling, effective delays, and in general estimation of connectivity with time-shift surrogates (Chapter 3). Finally we compute the same comparison with real data from a recording of neuronal spiking measured in an epilepsy patient (Chapter 4). We show that in this more complicated setting the advantages of applying a complex nonlinear technique such as the measure L over the simpler cross-correlogram and spike train distances are not so clear. In fact, at short time scales (tens of ms) the linear measures find more significant connections than L, despite the high sensitivity of L found for simulated Hindmarsh-Rose data.

The nonlinear measure L is an extension of a technique developed for

time-continuous signals in the framework of the study of low-dimensional chaotic systems [18] to point processes. In the case of continuous signals, the distance matrices are computed based on Taken's embedding theorem [122]. The idea is that inaccessible degrees of freedom are coupled into the observable variable via the system dynamics [109]. In the case of point processes, the distance matrix is not the result of a reconstruction. Sauer [109] extracted spike trains from a Rössler or Lorenz dynamical system through an integrate-and-fire model, showing that this leads to a one-to-one correspondence between the system states and interspike interval vectors of sufficiently large dimension. In the case of measure L, we do not use interspike intervals for reconstructions, because in that way we would not have simultaneous states for the pairs of dynamics. In [7], the authors underline that for the measure L there is a conceptual advantage in using distances between segments of spike trains because we can focus on spike rate or timing and also achieve a better sensitivity for determinism across different dynamics. In Chapter 2 we show that indeed the two spike train distances (ISI-and SPIKE-distance) have different sensitivity for different regimes of Hindmarsh-Rose dynamics, and in Chapter 3 this behavior was confirmed also with the use of time shifts and surrogates. The theory of recurrence plots [29] can be a relevant topic for future research for evaluating from the distance matrix whether it is meaningful to proceed with the measure L to check causality. In fact, recurrence plots correspond to the distance matrices that we compute for L but with the application of a threshold. Using the fact that distance matrices have the same properties regardless if they are computed from a point process or continuous signal, the same techniques can be adopted for both cases [26, 42, 47, 74].

The application of sophisticated mathematical techniques to reveal deterministic structures and nonlinear interdependence in spike trains needs much more study. First, we lack a more robust mathematical framework specific for the case of point processes. This would also help in the assessment of deterministic structures in the spike train signals [7], to be able to judge when the signals are suitable to be studied with techniques derived from the study of low-dimensional chaotic dynamics. Second, prominent problems known from the study of time-continuous signals, also affect the analysis of spike trains [17]. For example, in the study of causality between signals with different frequency distributions, there are issues in the choice of the parameters used for reconstruction, and it is very hard also to correctly estimate coupling strength [20, 64]. This aspect is even more important for spike trains, because the rate is related to the amount of information

present in the data [106]. This is similar for continuous signals where a dynamics with low frequency spectrum need to be recorded for long time in order to cover sufficiently the state space. Another complex problem is the detection of coupling with delay. In the context of continuous signals, many extensions of methods have been proposed [22, 34, 128], and time shift techniques have been applied and tested [129]. Nevertheless, there are still open issues to be solved [23]. In the study of point processes, we have shown that taking small delays in the coupling into account improves the detection of directionality for the nonlinear measure L, but the capability of the measure to consistently estimate coupling delay still needs to be tested.

Neuronal data are among the most complex signals to study. In fact single units recording are subject to common rhythms of different frequencies depending on the states, and correlated activity in populations of neurons have shown to play important roles [25, 98]. Furthermore, there is hierarchical network structure with few hub neurons spiking more than the others, and a long tail distribution of firing rate of different neurons. Firing rates of principal neurons show a lognormal-like distribution in all brain states [76]. Neuronal activity exhibits large variability on time scales ranging over seconds to days [75]. From a data analysis point of view it is a real challenge to analyze the connectivity from this kind of dataset. Models that incorporate these characteristics are needed for testing and developing new data analysis methods suited for facing these challenges. In particular, these models need to take into account different patterns of synchronization and desynchronization between units [8], and possibly also interactions between networks of neurons [9]. We have shown that initially it may be better to apply simple linear measures to get information about the systems, but it is important to take into account the nonlinearity of the neurons [32]. In fact, in the brain nonlinearity is already introduced on the cellular level given that the dynamical behavior of individual neurons is governed by integration, threshold, and saturation phenomena [66, 85]. An interesting aspect that deserves future study is the comparison between nonlinear methods derived from nonlinear chaotic dynamics, with other nonlinear methods from information theoretical approaches [46].

Here we have focussed on neuronal signals, but the measure L for point processes seems to be a very promising tool also for applications outside of neuroscience, for example in climatology [12, 60] or earthquake prediction [44]. In closing, we would like to point out that we provide the Matlab

source codes to calculate L and the spike train distances used here *.

*http://ntsa.upf.edu/downloads, http://www.fi.isc.cnr.it/users/thomas.kreuz/sourcecode.html

---

Adaptive measures of spike train synchrony

In this Appendix we summarize our study [107]:
E. Satuvuori, I. Malvestio, and T. Kreuz. *Measures of spike train synchrony and directionality*. In Mathematical and Theoretical Neuroscience: Cell, Network and Data analysis, pages 201−222. Springer INdAM series, 2017.

We describe the adaptive version of spike train distance that we use in Chapters 2, 3 and 4. Note that the similarity measures A-ISI-distance and A-SPIKE-distance are implemented in three publicly available software packages, the Matlab-based graphical user interface SPIKY[†] [59], cSPIKE[‡] (Matlab command line with MEX-files), and the open-source Python library PySpike[§] [78].

A.1   Introduction

Measures of spike train synchrony are estimators of the similarity between two or more spike trains, which are important tools for many applications in neuroscience. Among others, they allow to test the performance of neuronal models [48], they can be used to quantify the reliability of neuronal

---

[†]http://www.fi.isc.cnr.it/users/thomas.kreuz/Source-Code/SPIKY.html
[‡]http://www.fi.isc.cnr.it/users/thomas.kreuz/Source-Code/cSPIKE.html
[§]http://mariomulansky.github.io/PySpike

responses upon repeated presentations of a stimulus [72], and they help in the understanding of neural networks and neural coding [126, 127]. They have been used also outside neuroscience, for example in robotics [31] and prosthesis control [27].

Over the years many different methods have been developed in order to quantify spike train synchrony. They can be divided in two classes: time-scale dependent and time-scale independent methods. The two most known time-scale dependent methods are the Victor-Purpura distance [127] and the van Rossum distance [125]. They describe spike train (dis)similarity based on a user-given time-scale to which the measures are mainly sensitive to. Time scale independent methods have been developed more recently. In particular, the ISI-distance [58] and the SPIKE-distance [55, 56] are parameter-free distances, with the capability of discerning similarity across different spatial scales. These measures are time-resolved, so they are able to analyze the time dependence of spike train similarity.

One problematic aspect of time-scale independent methods is that they consider all time-scales as equally important. However, in real data one typically is not interested in the very small time scales. Especially in the presence of bursts (multiple spikes emitted in rapid succession), a more adaptive approach that gradually disregards differences in smaller time-scales is needed. Thus, here we describe the recently developed adaptive extensions of these parameter-free distances: A-ISI-distance and A-SPIKE-distance [108].

All of these similarity measures are symmetric and in consequence invariant to changes in the order of spike trains.

Two of the most well known spike train distances, the Victor-Purpura [127] and the van Rossum distance [125], are time-scale dependent. One drawback of these methods is the fixed time-scale, since it sets a boundary between rate and time coding for the whole recording. In the presence of bursts, where multiple spikes are emitted in rapid succession, there are usually many time-scales in the data and this is difficult to detect when using a measure that is sensitive to only one time-scale at a time [19].

The problem of having to choose one time-scale has been eliminated in the time-scale independent ISI-distance [58] and SPIKE-distance [55, 56], since these methods always adapt to the local firing rate. The ISI-distance and the SPIKE-distance are time resolved, time-scale free measures of dissimilarity between two or more spike trains. The ISI-distance is a measure of rate dissimilarity. It uses the interspike intervals (ISIs) to estimate local firing rate of spike trains and measures time-resolved differences between

them. The SPIKE-distance, on the other hand, compares spike time accuracy between the spike trains and uses local firing rates to adapt to the time-scale.

The ISI-distance and SPIKE-distance are looking at all time-scales at the same time. However, in real data not all time-scales are equally important, and this can lead to spuriously high values of dissimilarity when looking only at the local information. Many sequences of discrete events contain different time-scales. For example, in neuronal recordings besides regular spiking one often finds bursts, i.e. rapid successions of many spikes. The A-ISI-distance and the A-SPIKE-distance [108] are generalized versions of previously published methods the ISI-distance [57] and the SPIKE-distance [55]. The generalized measures also contain a notion of global context that discriminates between relative importance of differences in the global scale. This is done by means of a normalization based on a minimum relevant time-scale (MRTS). They start to gradually ignore differences between spike trains for interspike intervals (ISIs) that are smaller than the MRTS. The generalization provided by the MRTS is implemented with the threshold parameter thr, which is then applied in a different way to each of the measures. The threshold is used to determine if a difference between the spike trains should be assessed in a local or in a global context. This threshold is used for all three measures, but the way it is applied varies. The extended methods fall back to the original definitions when $thr = 0$ and we refer to this whenever we talk of the original methods. In this case even the smallest time-scales matter and all differences are assessed in relation to their local context only.

Throughout this Appendix we denote the number of spike trains by N, indices of spike trains by n and m, spike indexes by i and j and the number of spikes in spike train n by M_n. The spike times of spike train n are denoted by $\{t_i^{(n)}\}$ with $i = 1 \ldots M_n$.

A.2 Adaptive ISI-distance

The A-ISI-distance [108] measures the instantaneous rate difference between spike trains (see Figure A.1a). It relies on a time-resolved profile, meaning that in a first step a dissimilarity value is assigned to each time instant. To obtain this profile, we first assign to each time instant t the times of the previous spike and the following spike
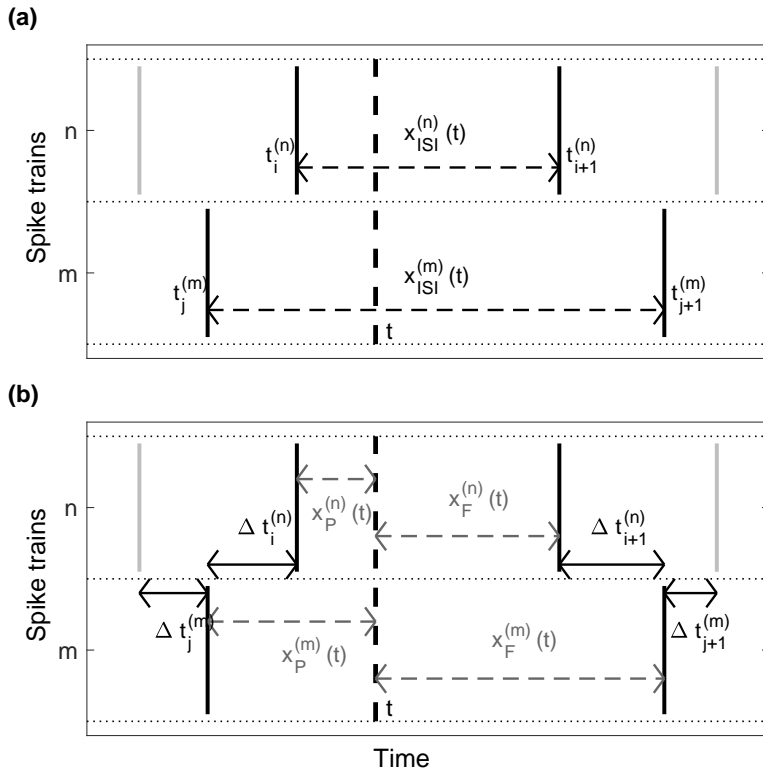
Figure A.1: Schematic drawing for all three measures. (a) Illustration of the variables used to define the **A-ISI-distance**. All measures use the instantaneous interspike interval $x_{ISI}^{(n)}(t)$ to adapt to the local firing rate. (b) Additional variables used for the **A-SPIKE-distance**.
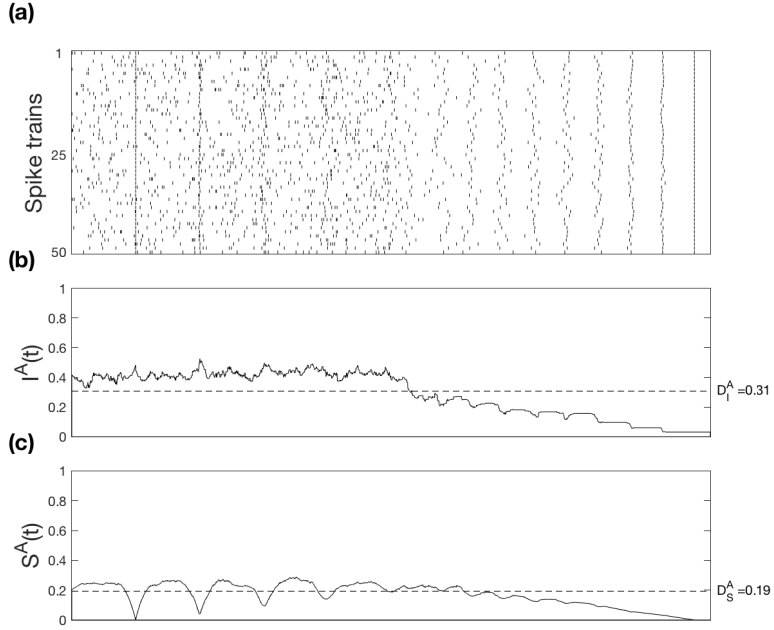
Figure A.2: Profiles of **A-ISI-distance** (a) and **A-SPIKE-distance** (b) for an artificial example dataset of 50 spike trains with population events with different jitters and decreasing noise over time.

$$t_{\mathrm{P}}^{(n)}(t) = \max\{t_i^{(n)} | t_i^{(n)} \leq t\} \quad \text{for} \quad t_1^{(n)} \leq t \leq t_{M_n}^{(n)} \tag{A.2.1}$$

$$t_{\mathrm{F}}^{(n)}(t) = \min\{t_i^{(n)} | t_i^{(n)} > t\} \quad \text{for} \quad t_1^{(n)} \leq t \leq t_{M_n}^{(n)}. \tag{A.2.2}$$

From this for each spike train n an instantaneous ISI can be calculated as

$$x_{\mathrm{ISI}}^{(n)}(t) = t_{\mathrm{F}}^{(n)}(t) - t_{\mathrm{P}}^{(n)}(t). \tag{A.2.3}$$

The A-ISI-profile is defined as a normalized instantaneous ratio in ISIs:

$$I_{n,m}^A(t) = \frac{|x_{\mathrm{ISI}}^{(n)}(t) - x_{\mathrm{ISI}}^{(m)}(t)|}{\max\{x_{\mathrm{ISI}}^{(n)}(t), x_{\mathrm{ISI}}^{(m)}(t), thr\}}. \tag{A.2.4}$$

For the A-ISI-distance the MRTS is defined so that when the ISI of both spike trains are smaller than a threshold value thr, the threshold value is used instead. The multivariate A-ISI-profile is obtained by averaging over all pairwise A-ISI-profiles:

$$I^A(t) = \frac{1}{N(N-1)/2} \sum_{n=1}^{N-1} \sum_{m=n+1}^{N} I_{n,m}^A(t). \qquad \text{(A.2.5)}$$

This is a non-continuous piecewise constant profile and integrating over time gives the A-ISI-distance:

$$D_I^A = \frac{1}{t_e - t_s} \int_{t_s}^{t_e} I^A(t)dt. \qquad \text{(A.2.6)}$$

Where t_s and t_e are the start and end times of the recording respectively. If thr is set to zero, the method falls back to the ISI-distance [57].

Figure A.2a shows an artificial spike train dataset together with the corresponding A-ISI-profile in Figure A.2b. The A-ISI-profile for the example dataset shows high dissimilarity for the left side of the raster plot, where noise is high. When the noise is decreased and rates become more similar in the right side, the dissimilarity profile goes down. The overall ISI-distance is the mean value of the profile.

A.3 Adaptive SPIKE-distance

The A-SPIKE-distance [108] measures the accuracy of spike times between spike trains relative to local firing rates (see Figure A.1b). In order to assess the accuracy of spike events, each spike is assigned a distance to its nearest neighbour in the other spike train:

$$\Delta t_i^{(n)} = \min_j(|t_i^{(n)} - t_j^{(m)}|). \qquad \text{(A.3.1)}$$

The distances are interpolated between spikes using for all times t the time differences to the previous and to the following spikes $x_P^{(n)}(t)$ and $x_F^{(n)}(t)$:

$$x_P^{(n)}(t) = t - t_i^{(n)} \quad \text{for} \quad t_i^{(n)} \leqslant t \leqslant t_{i+1}^{(n)} \qquad \text{(A.3.2)}$$

$$x_F^{(n)}(t) = t_{i+1}^{(n)} - t \quad \text{for} \quad t_i^{(n)} \leqslant t \leqslant t_{i+1}^{(n)}. \qquad \text{(A.3.3)}$$

These equations provide time-resolved quantities needed to define time-resolved dissimilarity profile from discrete values the same way as Eqs. A.2.1 and A.2.2 provide them for A-ISI-distance. The weighted spike time

difference for a spike train is then calculated as an interpolation from one difference to the next by

$$S_n(t) = \frac{\Delta t_i^{(n)}(t) x_F^{(n)}(t) + \Delta t_{i+1}^{(n)}(t) x_P^{(n)}(t)}{x_{\text{ISI}}^{(n)}(t)} \quad, \quad t_i^{(n)} \leqslant t \leqslant t_{i+1}^{(n)}. \quad \text{(A.3.4)}$$

This continuous function is analogous to term $x_{\text{ISI}}^{(n)}$ for the ISI-distance, except that it is piecewise linear instead of piecewise constant. The pairwise A-SPIKE-distance profile is calculated by temporally averaging the weighted spike time differences, normalizing to the local firing rate average and, finally, weighting each profile by the instantaneous firing rates of the two spike trains:

$$S_{m,n}^A(t) = \frac{S_n x_{\text{ISI}}^m(t) + S_m x_{\text{ISI}}^n(t)}{2 \langle x_{\text{ISI}}^{n,m}(t) \rangle \max\{\langle x_{\text{ISI}}^{n,m}(t) \rangle, thr\}}, \quad \text{(A.3.5)}$$

where $\langle x_{\text{ISI}}^{n,m}(t) \rangle$ is the mean over the two instantaneous ISIs. MRTS is defined by using a threshold, that replaces the denominator of weighting to spike time differences if the mean is smaller than the thr. This profile is analogous to the pairwise A-ISI-profile $I_{n,m}^A(t)$, but again it is piecewise linear, not piecewise constant. Unlike $S_n(t)$ it is not continuous, typically it exhibits instantaneous jumps at the times of the spikes. The multivariate A-SPIKE-profile is obtained the same way as the multivariate A-ISI-profile, by averaging over all pairwise profiles:

$$S^A(t) = \frac{1}{N(N-1)/2} \sum_{n=1}^{N-1} \sum_{m=n+1}^{N} S_{m,n}^A(t). \quad \text{(A.3.6)}$$

The final A-SPIKE-distance is calculated as the time integral over the multivariate A-SPIKE-profile the same way as the A-ISI-distance:

$$D_S^A = \frac{1}{t_e - t_s} \int_{t_s}^{t_e} S^A(t) dt. \quad \text{(A.3.7)}$$

The effect of applying the threshold can be seen in Figure A.3. With $thr = 0$ the method falls back to the regular SPIKE-distance [55]. The A-SPIKE-profile for the artificial test dataset in Figure A.2c goes to zero when the spikes in all spike trains appear at the exactly same time.
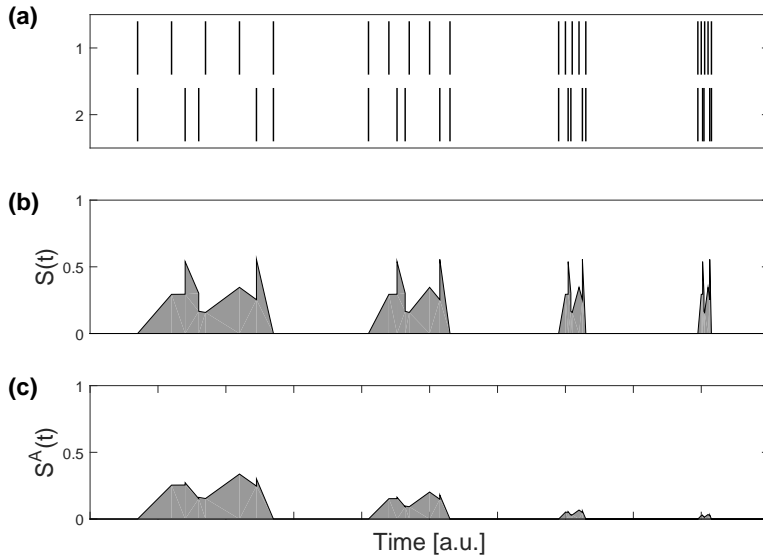
Figure A.3: An example spike train pair and its SPIKE-distance and A-SPIKE-distance profiles. (a) Two spike trains having four events with five spikes per event in each spike train. The sequence of spikes in all four events is the same but the event is increasingly compressed. The only thing that changes is the time-scale. From a global perspective the first event consists of non-synchronous individual spikes, while the last event consists of coincident bursts. The two events in the middle are intermediates. (b) The SPIKE-distance $S(t)$ looks only at the local context and has the same profile shape for all events. (c) The A-SPIKE-distance considers also the global context and judges the first event like the SPIKE-distance as being dissimilar, but scales down the small spike time differences in the burst and considers the coincident burst as very similar.

A.4 Selecting the threshold value

In some cases spikes that occur less than a second apart might be considered more simultaneous than those taking place within minutes, and in applications like meteorological systems, weeks instead of months. Setting the minimum relevant time-scale might not be a simple task. If no information of the system producing the spikes is available, all one can do to estimate an appropriate threshold value is to look at the ISIs.

There are two criteria that a threshold value extracted from the data has to fulfil. First of all it needs to adapt to changes in spike count so that adding more spikes gives shorter threshold. Additionally we want the threshold to adapt to changes in the ISI-distribution when the spike count is fixed. The more pronounced bursts are found in the data, the more likely any differences within aligned bursts are not as important as their placement. Thus, we want our threshold to get longer if the spikes are packed together. To do so, all the ISIs in all spike trains are pooled and the threshold is determined from the pooled ISI distribution.

One should not just take a value based on ISI-distribution that counts the interspike intervals, as the mean does, but weight them by their length, which is equivalent to taking the average of the second moments of ISIs. Doing this reduces the importance of very short ISIs even if they are statistically much more common. In order to obtain a value with the right dimension, the square root of the average must be taken:

$$thr = \sqrt{\langle (L_{\text{ISI}})^2 \rangle} = \sqrt{\frac{\sum_{n=1}^{N} a_n L_{\text{ISI}}^{n\,2}}{\sum_{n=1}^{N} a_n}}. \qquad (A.4.1)$$

Here we denoted a single ISI length in the pooled distribution as L_{ISI}^n and the number of ISI with length L_{ISI}^n as a_n. It is important to note, however, that this is only an estimate based on different time-scales found in the data. The selected MRTS is not an indicator of a time-scale of the system that produced the spikes.

As an example of how the threshold works we apply the threshold to Gamma $\Gamma(k, x)$ distribution. Since the kurtosis of the distribution is proportional to $1/k$, for small k the distribution contains large number of small ISI and few long ones. This is the property the threshold is tracking. Thus the mean of a gamma distribution is k/x and the second moment $(k+1)k/x$. thus the ratio of the threshold and the mean ISI is $thr/\langle L_{\text{ISI}} \rangle = \sqrt{x(k+1)/k}$. From the formula we can see that for small k, where the

distribution is more skewed, the ratio between the mean ISI and the threshold increases. This means that mainly the rare and large inter-burst ISIs are taken into account.

The threshold value determines the outcome of the adaptive methods. However, the threshold is not a hard set limiter neglecting everything below the threshold, but rather the point from which on differences are considered in a global instead of a local context.

References

[1] H. D. I. Abarbanel, N. F. Rulkov, and M. M. Sushchik. Generalized synchronization of chaos: The auxiliary system approach. *Physical Review E*, 53(5):4528, 1996.

[2] A. M. Aertsen and G. L. Gerstein. Evaluation of neuronal connectivity: sensitivity of cross-correlation. *Brain Research*, 340(2):341–354, 1985.

[3] G. Alba, E. Pereda, S. Mañas, L. D. Méndez, M. R. Duque, A. González, and J. J. González. The variability of eeg functional connectivity of young adhd subjects in different resting states. *Clinical Neurophysiology*, 127(2):1321–1330, 2016.

[4] R. G. Andrzejak, D. Chicharro, K. Lehnertz, and F. Mormann. Using bivariate signal analysis to characterize the epileptic focus: The benefit of surrogates. *Physical Review E*, 83(4):046203, 2011.

[5] R. G. Andrzejak, A. Kraskov, H. Stögbauer, F. Mormann, and T. Kreuz. Bivariate surrogate techniques: necessity, strengths, and caveats. *Physical Review E*, 68(6):066202, 2003.

[6] R. G. Andrzejak and T. Kreuz. Characterizing unidirectional couplings between point processes and flows. *EPL (Europhysics Letters)*, 96(5):50012, 2011.

[7] R. G. Andrzejak, F. Mormann, and T. Kreuz. Detecting determinism from point processes. *Physical Review E*, 90(6):062906, 2014.

[8] R. G. Andrzejak, G. Ruzzene, and I. Malvestio. Generalized synchronization between chimera states. *Chaos: An Interdisciplinary Journal of Nonlinear Science*, 27(5):053114, 2017.

[9] R. G. Andrzejak, G. Ruzzene, I. Malvestio, K. Schindler, E. Schöll, and A. Zakharova. Mean field phase synchronization between chimera states. *Chaos: An Interdisciplinary Journal of Nonlinear Science*, 28(9):091101, 2018.

[10] J. Arnhold, P. Grassberger, K. Lehnertz, and C. E. Elger. A robust method for detecting interdependences: application to intracranially recorded eeg. *Physica D: Nonlinear Phenomena*, 134(4):419–430, 1999.

[11] T. Bockhorst and U. Homberg. Amplitude and dynamics of polarization-plane signaling in the central complex of the locust brain. *Journal of neurophysiology*, 113(9):3291–3311, 2015.

[12] N. Boers, B. Bookhagen, H. M. Barbosa, N. Marwan, J. Kurths, and J. Marengo. Prediction of extreme floods in the eastern central andes based on a complex networks approach. *Nature communications*, 5:5199, 2014.

[13] N. Božanić. *Measures of spike train synchrony*. PhD thesis, Università degli Studi di Firenze, 2015.

[14] E. Bradley and H. Kantz. Nonlinear time-series analysis revisited. *Chaos: An Interdisciplinary Journal of Nonlinear Science*, 25(9):097610, 2015.

[15] A. Čenys, G. Lasiene, and K. Pyragas. Estimation of interrelation between chaotic observables. *Physica D: Nonlin. Phenom.*, 52(2):332–337, 1991.

[16] R. Cestnik and M. Rosenblum. Reconstructing networks of pulse-coupled oscillators from spike trains. *Physical Review E*, 96(1):012209, 2017.

[17] D. Chicharro. *Characterization of information and causality measures for the study of neuronal data*. PhD thesis, Universitat Pompeu Fabra, 2011.

[18] D. Chicharro and R. G. Andrzejak. Reliable detection of directional couplings using rank statistics. *Physical Review E*, 80(2):026217, 2009.

[19] D. Chicharro, T. Kreuz, and R. G. Andrzejak. What can spike train distances tell us about the neural code? *Journal of neuroscience methods*, 199(1):146–165, 2011.

[20] D. Chicharro and A. Ledberg. When two become one: the limits of causality analysis of brain dynamics. *PLoS One*, 7(3):e32466, 2012.

[21] E. Chornoboy, L. Schramm, and A. Karr. Maximum likelihood identification of neural point process systems. *Biological cybernetics*, 59(4-5):265–275, 1988.

[22] L. Cimponeriu, M. Rosenblum, and A. Pikovsky. Estimation of delay in coupling from time series. *Physical Review E*, 70(4):046213, 2004.

[23] D. Coufal, J. Jakubík, N. Jajcay, J. Hlinka, A. Krakovská, and M. Paluš. Detection of coupling delay: A problem not yet solved. *Chaos: An Interdisciplinary Journal of Nonlinear Science*, 27(8):083109, 2017.

[24] P. Dayan and L. F. Abbott. *Theoretical neuroscience*, volume 806. Cambridge, MA: MIT Press, 2001.

[25] J. de la Rocha, B. Doiron, E. Shea-Brown, K. Josić, and A. Reyes. Correlation between neural spike trains increases with firing rate. *Nature*, 448(7155):802–806, 2007.

[26] R. V. Donner, M. Small, J. F. Donges, N. Marwan, Y. Zou, R. Xiang, and J. Kurths. Recurrence-based time series analysis by means of complex network methods. *International Journal of Bifurcation and Chaos*, 21(04):1019–1046, 2011.

[27] S. Dura-Bernal, K. Li, S. A. Neymotin, J. T. Francis, J. C. Principe, and W. W. Lytton. Restoring behavior via inverse neurocontroller in a lesioned cortical spiking model driving a virtual arm. *Frontiers in neuroscience*, 10:28, 2016.

[28] R. Dzakpasu and M. Żochowski. Discriminating differing types of synchrony in neural systems. *Physica D: Nonlinear Phenomena*, 208(1-2):115–122, 2005.

[29] J.-P. Eckmann, S. O. Kamphorst, and D. Ruelle. Recurrence plots of dynamical systems. *EPL (Europhysics Letters)*, 4(9):973, 1987.

[30] G. B. Ermentrout, R. F. Galán, and N. N. Urban. Reliability, synchrony and noise. *Trends in neurosciences*, 31(8):428–434, 2008.

[31] A. Espinal, H. Rostro-Gonzalez, M. Carpio, E. I. Guerra-Hernandez, M. Ornelas-Rodriguez, H. J. Puga-Soberanes, M. A. Sotelo-Figuero, and P. Melin. Quadrupedal robot locomotion: A biologically inspired approach and its hardware implementation. *Computational Intelligence and Neuroscience*, 5615618, 2016.

[32] K. J. Friston. Brain function, nonlinear coupling, and neuronal transients. *Neuroscientist*, 7(5):406–418, 2001.

[33] K. J. Friston. Functional and effective connectivity: a review. *Brain connectivity*, 1(1):13–36, 2011.

[34] K. J. Friston, A. Bastos, V. Litvak, K. E. Stephan, P. Fries, and R. J. Moran. Dcm for complex-valued data: cross-spectra, coherence and phase-delays. *Neuroimage*, 59(1):439–455, 2012.

[35] H. Gast, J. Niediek, K. Schindler, J. Boström, V. A. Coenen, H. Beck, C. E. Elger, and F. Mormann. Burst firing of single neurons in the human medial temporal lobe changes before epileptic seizures. *Clinical neurophysiology*, 127(10):3329–3334, 2016.

[36] G. Girardeau, I. Inema, and G. Buzsáki. Reactivations of emotional memory in the hippocampus-amygdala system during sleep. *Nature Neuroscience*, 20(11):1634–1642, 2017.

[37] J. J. González, L. D. Méndez, S. Mañas, M. R. Duque, E. Pereda, and L. De Vera. Performance analysis of univariate and multivariate eeg measurements in the diagnosis of adhd. *Clin. Neurophysiol.*, 124(6):1139–1150, 2013.

[38] J. Goulet, J. L. van Hemmen, S. N. Jung, B. P. Chagnaud, B. Scholze, and J. Engelmann. Temporal precision and reliability in the velocity

regime of a hair-cell sensory system: the mechanosensory lateral line of gold-fish, carassius auratus. *Journal of neurophysiology*, 107(10):2581–2593, 2012.

[39] B. Gourévitch and J. J. Eggermont. Evaluating information transfer between auditory cortical neurons. *Journal of neurophysiology*, 97(3):2533–2543, 2007.

[40] R. E. Greenblatt, M. Pflieger, and A. Ossadtchi. Connectivity measures applied to human brain electrophysiological data. *Journal of neuroscience methods*, 207(1):1–16, 2012.

[41] S. Grün. Data-driven significance estimation for precise spike correlation. *Journal of neurophysiology*, 101(3):1126–1140, 2009.

[42] Y. Hirata and K. Aihara. Identifying hidden common causes from bivariate time series: a method using recurrence plots. *Physical Review E*, 81(1):016203, 2010.

[43] Y. Hirata, J. M. Amigó, Y. Matsuzaka, R. Yokota, H. Mushiake, and K. Aihara. Detecting causality by combined use of multiple methods: Climate and brain examples. *PloS one*, 11(7):e0158572, 2016.

[44] Y. Hirata, K. Iwayama, and K. Aihara. Possibility of short-term probabilistic forecasts for large earthquakes making good use of the limitations of existing catalogs. *Physical Review E*, 94(4):042217, 2016.

[45] K. Hlaváčková-Schindler, M. Paluš, M. Vejmelka, and J. Bhattacharya. Causality detection based on information-theoretic approaches in time series analysis. *Physics Reports*, 441(1):1–46, 2007.

[46] S. Ito, M. E. Hansen, R. Heiland, A. Lumsdaine, A. M. Litke, and J. M. Beggs. Extending transfer entropy improves identification of effective connectivity in a spiking cortical network model. *PloS one*, 6(11):e27431, 2011.

[47] J. S. Iwanski and E. Bradley. Recurrence plots of experimental data: To embed or not to embed? *Chaos: An Interdisciplinary Journal of Nonlinear Science*, 8(4):861–871, 1998.

[48] R. Jolivet, R. Kobayashi, A. Rauch, R. Naud, S. Shinomoto, and W. Gerstner. A benchmark test for a quantitative assessment of simple neuron models. *Journal of neuroscience methods*, 169(2):417–424, 2008.

[49] A. Kaiser and T. Schreiber. Nonparametric detection of dependences in stochastic point processes. *International Journal of Bifurcation and Chaos*, 14(06):1987–1993, 2004.

[50] N. Kasabov. To spike or not to spike: A probabilistic spiking neuron model. *Neural Networks*, 23(1):16–19, 2010.

[51] R. E. Kass, V. Ventura, and E. N. Brown. Statistical issues in the analysis of neuronal data. *Journal of neurophysiology*, 94(1):8–25, 2005.

[52] S. Kim, D. Putrino, S. Ghosh, and E. N. Brown. A granger causality measure for point process models of ensemble neural spiking activity. *PLoS computational biology*, 7(3):e1001110, 2011.

[53] L. Kocarev and U. Parlitz. Generalized synchronization, predictability, and equivalence of unidirectionally coupled dynamical systems. *Physical review letters*, 76(11):1816–1819, 1996.

[54] T. Kreuz. Measures of spike train synchrony. *Scholarpedia*, 6(10):11934, 2011.

[55] T. Kreuz, D. Chicharro, M. Greschner, and R. G. Andrzejak. Time-resolved and time-scale adaptive measures of spike train synchrony. *Journal of neuroscience methods*, 195(1):92–106, 2011.

[56] T. Kreuz, D. Chicharro, C. Houghton, R. G. Andrzejak, and F. Mormann. Monitoring spike train synchrony. *Journal of neurophysiology*, 109(5):1457–1472, 2012.

[57] T. Kreuz, J. S. Haas, A. Morelli, H. D. Abarbanel, and A. Politi. Measuring spike train synchrony. *Journal of neuroscience methods*, 165(1):151–161, 2007.

[58] T. Kreuz, F. Mormann, R. G. Andrzejak, A. Kraskov, K. Lehnertz, and P. Grassberger. Measuring synchronization in coupled model systems: A comparison of different approaches. *Physica D: Nonlinear Phenomena*, 225(1):29–42, 2007.

[59] T. Kreuz, M. Mulansky, and N. Bozanic. Spiky: A graphical user interface for monitoring spike train synchrony. *Journal of neurophysiology*, 113(9):3432–3445, 2015.

[60] T. Kreuz, E. Satuvuori, M. Pofahl, and M. Mulansky. Leaders and followers: quantifying consistency in spatio-temporal propagation patterns. *New Journal of Physics*, 19(4):043028, 2017.

[61] M. Krumin and S. Shoham. Multivariate autoregressive modeling and granger causality analysis of multiple spike trains. *Computational intelligence and neuroscience*, 2010:1–10, 2010.

[62] D. Kugiumtzis. Test your surrogate data before you test for nonlinearity. *Physical Review E*, 60(3):2808–2816, 1999.

[63] E. F. Kutter, J. Bostroem, C. E. Elger, F. Mormann, and A. Nieder. Single neurons in the human brain encode numbers. *Neuron*, 100(3):753–761, 2018.

[64] P. Laiou and R. G. Andrzejak. Coupling strength versus coupling impact in nonidentical bidirectionally coupled dynamics. *Physical Review E*, 95(1):012210, 2017.

[65] G. Lancaster, D. Iatsenko, A. Pidde, V. Ticcinelli, and A. Stefanovska. Surrogate data for hypothesis testing of physical systems. *Physics Reports*, 748:1–60, 2018.

[66] K. Lehnertz, C. Geier, T. Rings, and K. Stahn. Capturing time-varying brain dynamics. *EPJ Nonlinear Biomedical Physics*, 5:2, 2017.

[67] D. Levenstein, B. O. Watson, J. Rinzel, and G. Buzsáki. Sleep regulation of the distribution of cortical firing rates. *Current Opinion in Neurobiology*, 44:34–42, 2017.

[68] M. S. Lewicki. A review of methods for spike sorting: the detection and classification of neural action potentials. *Network*, 9(4):R53–R78, 1998.

[69] Z. Li, G. Ouyang, D. Li, and X. Li. Characterization of the causality between spike trains with permutation conditional mutual information. *Physical Review E*, 84(2):021929, 2011.

[70] S. G. Louis, M. Diesmann, et al. Surrogate spike train generation through dithering in operational time. *Frontiers in computational neuroscience*, 4:127, 2010.

[71] J. H. Macke, P. Berens, A. S. Ecker, A. S. Tolias, and M. Bethge. Generating spike trains with specified correlation coefficients. *Neural computation*, 21(2):397–423, 2009.

[72] Z. F. Mainen and T. J. Sejnowski. Reliability of spike timing in neocortical neurons. *Science*, 268(5216):1503–1506, 1995.

[73] I. Malvestio, T. Kreuz, and R. G. Andrzejak. Robustness and versatility of a nonlinear interdependence method for directional coupling detection from spike trains. *Physical Review E*, 96(2):022203, 2017.

[74] N. Marwan, M. Carmen Romano, M. Thiel, and J. Kurths. Recurrence plots for the analysis of complex systems. *Physics Reports*, 438(5-6):237–329, 2007.

[75] A. Mazaheri, H. A. Slagter, G. Thut, and J. J. Foxe. Orchestration of brain oscillations: principles and functions. *European Journal of Neuroscience*, 48(7):2385–2388, 2018.

[76] K. Mizuseki and G. Buzsáki. Preconfigured, skewed distribution of firing rates in the hippocampus and entorhinal cortex. *Cell Reports*, 4(5):1010–1021, 2013.

[77] M. Mulansky, N. Bozanic, A. Sburlea, and T. Kreuz. A guide to time-resolved and parameter-free measures of spike train synchrony. In *Event-based Control, Communication, and Signal Processing (EBCCSP), 2015 International Conference on*, pages 1–8. IEEE, 2015.

[78] M. Mulansky and T. Kreuz. Pyspike - A python library for analyzing spike train synchrony. *Software X*, 5:183, 2016.

[79] R. Narayan, G. Graña, and K. Sen. Distinct time scales in cortical discrimination of natural sounds in songbirds. *Journal of neurophysiology*, 96(1):252–258, 2006.

[80] D. Naro, C. Rummel, K. Schindler, and R. G. Andrzejak. Detecting determinism with improved sensitivity in time series: Rank-based

nonlinear predictability score. *Physical Review E*, 90(3):032913, 2014.

[81] A. G. Nedungadi, G. Rangarajan, N. Jain, and M. Ding. Analyzing multiple spike trains with nonparametric granger causality. *J. Comput. Neurosci.*, 27(1):55–64, 2009.

[82] J. Niediek, J. Boström, C. E. Elger, and F. Mormann. Reliable analysis of single-unit recordings from the human brain under noisy conditions: tracking neurons over hours. *PloS one*, 11(12):e0166598, 2016.

[83] D. Nikolić, R. C. Mureşan, W. Feng, and W. Singer. Scaled correlation analysis: A better way to compute a cross-correlogram. *European Journal of Neuroscience*, 35(5):742–762, 2012.

[84] Y. Nir, R. J. Staba, T. Andrillon, V. V. Vyazovskiy, C. Cirelli, I. Fried, and G. Tononi. Regional Slow Waves and Spindles in Human Sleep. *Neuron*, 70(1):153–169, 2011.

[85] P. L. Nunez, R. Srinivasan, et al. *Electric fields of the brain: the neurophysics of EEG*. Oxford University Press, USA, 2006.

[86] S. Oba, K. Nakae, Y. Ikegaya, S. Aki, J. Yoshimoto, and S. Ishii. Empirical Bayesian significance measure of neuronal spike response. *BMC Neuroscience*, 17(1):27, 2016.

[87] M. Okatan, M. A. Wilson, and E. N. Brown. Analyzing functional connectivity using a network likelihood model of ensemble neural spiking activity. *Neural computation*, 17(9):1927–1961, 2005.

[88] U. Olcese, J. J. Bos, M. Vinck, J. V. Lankelma, L. B. van Mourik-Donga, F. Schlumm, and C. M. Pennartz. Spike-based functional connectivity in cerebral cortex and hippocampus: loss of global connectivity is coupled to preservation of local connectivity during non-rem sleep. *Journal of Neuroscience*, 36(29):7676–7692, 2016.

[89] J. G. Orlandi, O. Stetter, J. Soriano, T. Geisel, and D. Battaglia. Transfer entropy reconstruction and labeling of neuronal connections from simulated calcium imaging. *PloS one*, 9(6):e98842, 2014.

[90] M. Paluš and M. Vejmelka. Directionality of coupling from bivariate time series: How to avoid false causalities and missed connections. *Physical Review E*, 75(5):056211, 2007.

[91] P. Papiotis, M. Maestre, M. Marchini, and A. Perez. Synchronization of intonation adjustments in violin duets; towards an objective evaluation of musical interaction. In *Proceedings of the 14th conference in Digital Audio Effects (DAFx-11)*, 2011.

[92] I. Park, A. R. Paiva, T. B. DeMarse, and J. C. Príncipe. An efficient algorithm for continuous time cross correlogram of spike trains. *Journal of Neuroscience methods*, 168(2):514–523, 2008.

[93] E. Pereda, R. Quian Quiroga, and J. Bhattacharya. Nonlinear multivariate analysis of neurophysiological signals. *Progress in Neurobiology*, 77(1):1–37, 2005.

[94] D. H. Perkel, G. L. Gerstein, and G. P. Moore. Neuronal Spike Trains and Stochastic Point Processes: I. The Single Spike Train. *Biophysical Journal*, 7(4):391–418, 1967.

[95] D. H. Perkel, G. L. Gerstein, and G. P. Moore. Neuronal Spike Trains and Stochastic Point Processes: II. Simultaneous Spike Trains. *Biophysical Journal*, 7(4):419–440, 1967.

[96] V. Pernice and S. Rotter. Reconstruction of sparse connectivity in neural networks from spike train covariances. *Journal of Statistical Mechanics: Theory and Experiment*, 2013(03):P03008, 2013.

[97] A. Pikovsky. Reconstruction of a neural network from a time series of firing rates. *Physical Review E*, 93(6):062313, 2016.

[98] J. W. Pillow, J. Shlens, L. Paninski, A. Sher, A. M. Litke, E. Chichilnisky, and E. P. Simoncelli. Spatio-temporal correlations and visual signalling in a complete neuronal population. *Nature*, 454(7207):995–999, 2008.

[99] R. D. Pinto, P. Varona, A. R. Volkovskii, A. Szücs, H. D. I. Abarbanel, and M. I. Rabinovich. Synchronous behavior of two coupled electronic neurons. *Phys. Rev. E*, 62(2):2644, 2000.

[100] R. Quian Quiroga, J. Arnhold, and P. Grassberger. Learning driver-response relationships from synchronization patterns. *Physical Review E*, 61(5):5142–5148, 2000.

[101] T. P. Reber, J. Faber, J. Niediek, J. Boström, C. E. Elger, and F. Mormann. Single-Neuron Correlates of Conscious Perception in the Human Medial Temporal Lobe. *Current Biology*, 27(19):2991–2998, 2017.

[102] R. Rial, J. González, L. Gené, M. Akaârir, S. Esteban, A. Gamundí, P. Barceló, and C. Nicolau. Asymmetric sleep in apneic human patients. *American Journal of Physiology-Regulatory, Integrative and Comparative Physiology*, 304(3):R232–R237, 2012.

[103] A. Roebroeck, E. Formisano, and R. Goebel. The identification of interacting networks in the brain using fmri: model selection, causality and deconvolution. *Neuroimage*, 58(2):296–302, 2011.

[104] M. G. Rosenblum and A. S. Pikovsky. Detecting direction of coupling in interacting oscillators. *Physical Review E*, 64(4):045202, 2001.

[105] N. F. Rulkov, M. M. Sushchik, L. S. Tsimring, and H. D. I. Abarbanel. Generalized synchronization of chaos in directionally coupled chaotic systems. *Physical Review E*, 51(2):980–994, 1995.

[106] E. Satuvuori and T. Kreuz. Which spike train distance is most suitable for distinguishing rate and temporal coding? *Journal of neuroscience methods*, 299:22–33, 2018.

[107] E. Satuvuori, I. Malvestio, and T. Kreuz. Measures of spike train synchrony and directionality. In *Mathematical and Theoretical Neuroscience: Cell, Network and Data analysis*, pages 201–222. Springer INdAM series, 2017.

[108] E. Satuvuori, M. Mulansky, N. Bozanic, I. Malvestio, F. Zeldenrust, K. Lenk, and T. Kreuz. Measures of spike train synchrony for data with multiple time scales. *Journal of neuroscience methods*, 287:25–38, 2017.

[109] T. Sauer. Reconstruction of dynamical systems from interspike intervals. *Physical Review Letters*, 72(24):3811–3815, 1994.

[110] C. A. Schevon, S. A. Weiss, G. McKhann, R. R. Goodman, R. Yuste, R. G. Emerson, and A. J. Trevelyan. Evidence of an inhibitory restraint of seizure activity in humans. *Nature Communications*, 3:1011–1060, 2012.

[111] S. J. Schiff, P. So, T. Chang, R. E. Burke, and T. Sauer. Detecting dynamical interdependence and generalized synchrony through mutual prediction in a neural ensemble. *Physical Review E*, 54(6):6708–6724, 1996.

[112] T. Schreiber and A. Schmitz. Surrogate time series. *Physica D: Nonlinear Phenomena*, 142(3):346–382, 2000.

[113] J. P. Segundo. A history of spike trains as point processes in neural coding. *Journal of Physiology-Paris*, 104(3-4):156–159, 2010.

[114] J. P. Shaffer. Multiple hypothesis testing. *Annual review of psychology*, 46(1):561–584, 1995.

[115] D. A. Smirnov and R. G. Andrzejak. Detection of weak directional coupling: Phase-dynamics approach versus state-space approach. *Physical Review E*, 71(3):036207, 2005.

[116] E. H. Smith, J.-y. Liou, T. S. Davis, E. M. Merricks, S. S. Kellis, S. A. Weiss, B. Greger, P. A. House, G. M. McKhann II, R. R. Goodman, et al. The ictal wavefront is the spatiotemporal source of discharges during spontaneous human seizures. *Nature communications*, 7:11098, 2016.

[117] C. J. Stam. Nonlinear dynamical analysis of eeg and meg: review of an emerging field. *Clinical neurophysiology*, 116(10):2266–2301, 2005.

[118] B. Staude, S. Rotter, and S. Grün. Can spike coordination be differentiated from rate covariation? *Neural Computation*, 20(8):1973–1999, 2008.

[119] O. Stetter, D. Battaglia, J. Soriano, and T. Geisel. Model-free reconstruction of excitatory neuronal connectivity from calcium imaging signals. *PLoS computational biology*, 8(8):e1002653, 2012.

[120] I. H. Stevenson, J. M. Rebesco, L. E. Miller, and K. P. Körding. Inferring functional connections between neurons. *Current opinion in neurobiology*, 18(6):582–588, 2008.

[121] G. Sugihara, R. May, H. Ye, C.-h. Hsieh, E. Deyle, M. Fogarty, and S. Munch. Detecting Causality in Complex Ecosystems. *Science*, 338(6106):496–500, 2012.

[122] F. Takens. Detecting strange attractors in turbulence. In *Dynamical systems and turbulence, Warwick 1980*, pages 366–381. Springer, 1981.

[123] J. Theiler. Spurious dimension from correlation algorithms applied to limited time-series data. *Physical Review A*, 34(3):2427–2432, 1986.

[124] F. Van Bussel, B. Kriener, and M. Timme. Inferring synaptic connectivity from spatio-temporal spike patterns. *Frontiers in computational neuroscience*, 5:3, 2011.

[125] M. C. van Rossum. A novel spike distance. *Neural computation*, 13(4):751–763, 2001.

[126] J. D. Victor. Spike train metrics. *Current opinion in neurobiology*, 15(5):585–592, 2005.

[127] J. D. Victor and K. P. Purpura. Nature and precision of temporal coding in visual cortex: a metric-space analysis. *Journal of neurophysiology*, 76(2):1310–1326, 1996.

[128] M. Wibral, N. Pampu, V. Priesemann, F. Siebenhühner, H. Seiwert, M. Lindner, J. T. Lizier, and R. Vicente. Measuring information-transfer delays. *PloS one*, 8(2):e55809, 2013.

[129] H. Ye, E. R. Deyle, L. J. Gilarranz, and G. Sugihara. Distinguishing time-delayed causal interactions using convergent cross mapping. *Scientific Reports*, 5, 2015.

[130] L. Zapata-Fonseca, D. Dotov, R. Fossion, and T. Froese. Time-series analysis of embodied interaction: movement variability and complexity matching as dyadic properties. *Frontiers in psychology*, 7:1940, 2016.